Order 10^4 speedup in global linear instability analysis using matrix formation

Pedro Paredes *, Miguel Hermanns, Soledad Le Clainche, Vassilis Theofilis

School of Aeronautics, Universidad Politécnica de Madrid, Pza. Cardenal Cisneros 3, E-28040 Madrid, Spain

A B S T R A C T

A unified solution framework is presented for one-, two- or three-dimensional complex non-symmetric eigenvalue problems, respectively governing linear modal instability of incompressible fluid flows in rectangular domains having two, one or no homogeneous spatial directions. The solution algorithm is based on subspace iteration in which the spatial discretization matrix is formed, stored and inverted serially. Results delivered by spectral collocation based on the Chebyshev-Gauss–Lobatto (CGL) points and a suite of high-order finite-difference methods comprising the previously employed for this type of work Dispersion-Relation-Preserving (DRP) and Padé finite-difference schemes, as well as the Summation-by-parts (SBP) and the new high-order finite-difference scheme of order q (FD-q) have been compared from the point of view of accuracy and efficiency in standard validation cases of temporal local and BiGlobal linear instability. The FD-q method has been found to significantly outperform all other finite difference schemes in solving classic linear local, BiGlobal, and TriGlobal eigenvalue problems, as regards both memory and CPU time requirements. Results shown in the present study disprove the paradigm that spectral methods are superior to finite difference methods in terms of computational cost, at equal accuracy, FD-q spatial discretization delivering a speedup of $\mathcal{O}(10^4)$. Consequently, accurate solutions of the three-dimensional (TriGlobal) eigenvalue problems may be solved on typical desktop computers with modest computational effort.

1. Introduction

The present contribution focuses on the application of high-order finite-difference methods to the numerical solution of partial-derivative eigenvalue problems (EVP) which govern global linear flow instability. The term *global* instability is used here to collectively describe instability in domains in which the number of homogeneous spatial directions is one or zero, respectively corresponding to two- and three-dimensional EVP. Global linear instability analysis is motivated by the need to unravel the origins of laminar-turbulent transition in flows over or through complex geometries; the theory has advanced into a field of vigorous research activity in the last decade [1]. This endeavor has been facilitated by the wider availability of computational resources commensurate with the solution of the multi-dimensional eigenvalue and singular value decomposition problems underlying the theory. While non-modal studies of instability of complex flows have commenced appearing in the literature in recent years [e.g. 2,3], the overwhelming majority of work is performed in a modal context, governed by the solution of large-scale eigenvalue problems. Their solution entails two aspects, spatial discretization and eigenspectrum computation, which are briefly reviewed next.

Regarding spatial discretizations for global instability analysis, the early flow applications analyzed involved simple two-dimensional domains in which the numerical discretization techniques employed were straightforward extensions of those used in the solution of classic one-dimensional linear stability eigenvalue problems. The pioneering studies of inviscid instability of a vortex by Pierrehumbert [4], viscous instability analyses in the wake of the circular cylinder by Zebib [5] and the rectangular duct by Tatsumi and Yoshimura [6] fall in this category; all three works employed spectral methods for the spatial discretization of the linearized operator. Almost simultaneously, finite-element methods were also used for the solution of the two-dimensional EVP by Jackson [7] and Morzyński and Thiele [8], while finite-volume methods soon followed [9]. Although finite-element or finite-volume methods are not restricted to the single-domain two-dimensional grids employed in the early spectral analyses, their low formal order of accuracy needs to be compensated in terms of grid density: should sharp gradients need to be resolved, as the case is with the amplitude functions of global eigenmodes at increasingly high Reynolds numbers, one resorts to using unstructured meshes of ever-increasing density in order to achieve convergence [e.g. 10]. In doing so, one effectively trades off the efficiency of a high-order method in favor of the flexibility offered by the unstructured mesh discretization. The case is thus set for high-order accurate, flexible *and* efficient numerical methods in order to solve the BiGlobal EVP.

---

 * Corresponding author.
   E-mail address: pedro.paredes@upm.es (P. Paredes).

Such an approach has been introduced in the seminal work of three-dimensional instability in the wake of a circular cylinder by Barkley and Henderson [11,12] in the form of spectral-element discretization on structured meshes. The first application of a spectral/hp-element method [13] to the study of a global instability problem on unstructured meshes was that of Theofilis et al. [14], who recovered instability in the wake of a NACA0012 airfoil as the leading BiGlobal eigenmode of the steady wake flow.

Regarding eigenspectrum computations, early analyses relied on full eigenspectrum computation [15,5], which scales as $\mathcal{O}(M^2)$ and $\mathcal{O}(M^3)$ with regard to memory and CPU time requirements, respectively, if a total number of M degrees of freedom are used for the spatial discretization of the linearized operator. Both estimates present a severe limitation for full eigenspectrum computations in both two and three simultaneously discretized spatial directions. Access to the entire eigenspectrum of global eigenvalue problems is thus routinely sacrificed in present-day global instability analysis algorithms, which employ some form of subspace iteration to recover a small subset of the eigenspectrum. This practice is justified since, from a physical point of view only a relatively small part of the leading perturbations, those close to the origin, is relevant to flow instability. On the other hand access to the smallest eigenvalues implies inversion of the discretized linear operator; a common practice to avoid inversion, the cost of which is also $\mathcal{O}(M^2)$ and $\mathcal{O}(M^3)$ if a direct dense method is used, is to emulate the action of the inverse operator during the subspace creation, without ever forming or inverting the operator. Well-established practices in the latter context, collectively referred to as *time-stepping* methods, have been introduced by Eriksson and Rizzi [16] and Edwards et al. [17] and are in use in modern global instability analyses, such as the three-dimensional global instability analyses of Tezuka and Suzuki [18] and Bagheri et al. [19], or the modal and non-modal work of Blackburn et al. [20].

Nevertheless, it may be argued that forming the matrix has certain advantages over time-stepping, the main ones being simplicity in the formation of the global eigenvalue or singular value problem, and flexibility in extending the analysis into regimes that would require the availability of entirely different flow solvers, if the time-stepping approach were to be used. When the matrix is formed, it is straightforward to include in the same code compressibility effects in subsonic or supersonic flow, extend the analysis into the hypersonic regime by implementing a few additional terms in an otherwise unchanged algorithm, or include new physics, such as non-Newtonian dynamics or magnetohydrodynamics, all by appropriately modifying the linearized operator. The penalty to be paid is of course the need to store and operate large matrices which, as the resolution requirements increase, can quickly be unmanageable in all but the largest supercomputers.

For a given spatial discretization method within a matrix forming context, straightforward serial (see [21] and Supplemental Appendix 3 of [1] for an overview), as well as parallel computations (ranging from a modest number of processors [22] up to massively parallel EVP solutions [23–26]) have been used for the recovery of (part of) the global eigenspectrum. A key efficiency improvement was proposed by Crouch et al. [22] who first employed sparse direct solvers for this class of problems. In order to exploit the benefits of using sparse solvers, Merle et al. [27] compared Padé [28] and Dispersion-Relation-Preserving [29] high-order finite-difference spatial discretization schemes to the solution of the incompressible BiGlobal EVP and concluded that from a combined accuracy and efficiency perspective the DRP schemes offer the best alternative for the solution of this global EVP.

The present contribution revisits the numerical solution of the EVP arising in global linear stability theory using matrix formation and spatial discretization of the spatial operator by means of the previously employed Padé compact [28] and Dispersion-

Relation-Preserving [29] schemes, as well as standard high-order finite differences, Summation-By-Parts operators [30,31], and the less-known very high order finite difference schemes of Hermanns and Hernández [32]. All results are compared against those delivered by the spectral collocation method based on (standard and coordinate-transformed) Chebyshev Gauss–Lobatto grids. Although the main focus of the present work is global instability analysis in two or three inhomogeneous spatial directions, the one-dimensional EVP governing local flow stability is also solved, since its well-known highly accurate results assist quantification of the error associated with each spatial discretization method. The potential of the most accurate finite-difference method identified to permit transient growth analyses [33] is demonstrated also in this local linear stability limit. For the sake of quantifying errors in the numerical solution of the two- and three-dimensional global linear stability eigenvalue problem, solution of the Helmholtz equation in two and three spatial dimensions is also presented using the spatial discretization methods discussed earlier since, on the one hand analytically-known solutions exist for the Helmholtz EVP and on the other hand the Laplacian operator in two and three spatial dimensions is a key element in the construction of the respective BiGlobal and TriGlobal eigenvalue problems.

Section 2 exposes an introduction to some aspects of modal linear stability theory and the one, two- and three-dimensional stability problems solved in this paper. In Section 3, the high-order spatial discretization methods discussed earlier are briefly described. Their application to the numerical solution of the one-, two- and three-dimensional eigenvalue problems governing incompressible fluid flow stability is discussed in terms of accuracy and computational efficiency in Sections 4 and 5 respectively. Conclusions are offered in Section 6.

2. Modal linear stability theory

Hydrodynamic instability studies the behaviour of a laminar flow field, upon the introduction of small-amplitude perturbations, in order to improve the understanding of the processes involved in the onset of unsteadiness in moderate-Reynolds-number flows and the transition of laminar flow to a turbulent regime.

The vector of fluid variables $\mathbf{q} = [\mathbf{u}, p]^{\mathrm{T}}$ is decomposed into a steady base flow $\mathbf{Q} = [\mathbf{U}, P]^{\mathrm{T}}$ and an unsteady small disturbance or perturbation $\varepsilon\tilde{\mathbf{q}}$, with $\varepsilon \ll 1$ and $\tilde{\mathbf{q}} = [\tilde{\mathbf{u}}, \tilde{p}]^{\mathrm{T}}$:

$$\mathbf{q}(\mathbf{x}, t) = \mathbf{Q}(\mathbf{x}) + \varepsilon\tilde{\mathbf{q}}(\mathbf{x}, t). \tag{1}$$

Once this decomposition is assumed, solutions to the initial-value-problem

$$\frac{d\tilde{\mathbf{q}}}{dt} = \mathcal{L}(Re, \mathbf{Q})\tilde{\mathbf{q}}, \tag{2}$$

are sought. Specific comments on the dependence of these quantities on the spatial coordinates, $\mathbf{x}$, and time, t, will be made in what follows. The operator $\mathcal{L}$ is associated with the spatial discretization of the linearized Navier Stokes equations (LNSE) of motion and comprise the base state, $\mathbf{Q}(\mathbf{x})$, and its spatial derivatives. In case of steady base flows, the separability between time and space coordinates in (2) permits introducing a Fourier decomposition in time,

$$\tilde{\mathbf{q}}(\mathbf{x}, t) = \hat{\mathbf{q}}(\mathbf{x})\Theta(\mathbf{x}, t), \quad \Theta = \theta(\mathbf{x})\exp(-i\omega t) \tag{3}$$

with $\theta(\mathbf{x})$ a spatial phase function, which depends on the number of homogeneous directions of the problem, leading to the generalized matrix eigenvalue problem:

$$\mathcal{A}\hat{\mathbf{q}} = \omega\mathcal{B}\hat{\mathbf{q}}. \tag{4}$$

Here matrices $\mathcal{A}$ and $\mathcal{B}$ discretize the operator $\mathcal{L}$, with $\mathcal{B}$ being singular due to the continuity equation. The sought complex

eigenvalue is $\omega = \omega_r + i\omega_i$, the real part being a circular frequency, while the imaginary part being the temporal amplification/damping rate; and $\hat{\mathbf{q}}(\mathbf{x};t) = (\hat{\mathbf{u}}, \hat{p})^{\mathrm{T}}$ is the vector comprising the amplitude functions of linear velocity-component and pressure perturbations.

2.1. Local instability: one-dimensional LNSE

Throughout the largest part of last century, additional assumptions have been made to the base flow and the disturbances in order to make the problem solvable, the strongest of which was adopting the so-called parallel-flow assumption. The base flow is assumed to be homogeneous in two out of the three spatial directions, here x and z, and comprises components

$$\mathbf{Q} = [U, 0, W, P]^{\mathrm{T}}(y), \tag{5}$$

such that the coefficients of the resulting eigenvalue problem are x and z independent. Modal perturbations then get the form

$$\tilde{\mathbf{q}}(x, y, z, t) = \hat{\mathbf{q}}(y) \exp[\mathrm{i}(\alpha x + \beta z - \omega t)], \tag{6}$$

where the periodicity lengths $L_x = 2\pi/\alpha$ and $L_z = 2\pi/\beta$ are imposed to the disturbances' shapes in the x and z directions respectively.

Upon substitution of Eq. (6) into the LNSE, the operators $\mathcal{A}$ and $\mathcal{B}$ defining (4) become:

$$\mathcal{A}_{1D} = \begin{pmatrix} \mathcal{L}_{1D} & U_y & 0 & \mathrm{i}\alpha \\ 0 & \mathcal{L}_{1D} & 0 & \mathcal{D}_y \\ 0 & W_y & \mathcal{L}_{1D} & \mathrm{i}\beta \\ \mathrm{i}\alpha & \mathcal{D}_y & \mathrm{i}\beta & 0 \end{pmatrix}, \quad \mathcal{B}_{1D} = \begin{pmatrix} \mathrm{i} & 0 & 0 & 0 \\ 0 & \mathrm{i} & 0 & 0 \\ 0 & 0 & \mathrm{i} & 0 \\ 0 & 0 & 0 & 0 \end{pmatrix}, \tag{7}$$

where $\mathcal{L}_{1D} = \mathrm{i}\alpha U + \mathrm{i}\beta W - \frac{1}{Re}(\mathcal{D}_{yy} - \alpha^2 - \beta^2)$, $\mathcal{D}_y$ being the first derivative matrix and $\mathcal{D}_{yy}$ the second derivative matrix respect to y direction.

2.2. BiGlobal instability analysis: two-dimensional LNSE

Assuming that the base flow is now dependent on two out of the three spatial coordinates

$$\mathbf{Q} = [U, V, W, P]^{\mathrm{T}}(x, y), \tag{8}$$

the coefficients of the LNSE are z independent, and modal perturbations now get the form

$$\tilde{\mathbf{q}}(x, y, z, t) = \hat{\mathbf{q}}(x, y) \exp[\mathrm{i}(\beta z - \omega t)]. \tag{9}$$

The disturbances are still three-dimensional, but a sinusoidal dependence is assumed only in the homogeneous z direction, with the periodicity length $L_z = 2\pi/\beta$. Upon substitution of Eq. (9) into the LNSE, the PDE-based GEVP operators are

$$\mathcal{A}_{2D} = \begin{pmatrix} \mathcal{L}_{2D}+U_x & U_y & 0 & \mathcal{D}_x \\ V_x & \mathcal{L}_{2D}+V_y & 0 & \mathcal{D}_y \\ W_x & W_y & \mathcal{L}_{2D} & \mathrm{i}\beta \\ \mathcal{D}_x & \mathcal{D}_y & \mathrm{i}\beta & 0 \end{pmatrix}, \quad \mathcal{B}_{2D} = \begin{pmatrix} \mathrm{i} & 0 & 0 & 0 \\ 0 & \mathrm{i} & 0 & 0 \\ 0 & 0 & \mathrm{i} & 0 \\ 0 & 0 & 0 & 0 \end{pmatrix}, \tag{10}$$

where $\mathcal{L}_{2D} = U\mathcal{D}_y + V\mathcal{D}_y + \mathrm{i}\beta W - \frac{1}{Re}(\mathcal{D}_{xx} + \mathcal{D}_{yy} - \beta^2)$, $\mathcal{D}_x$ being the first derivative matrix and $\mathcal{D}_{xx}$ the second derivative matrix respect to x direction.

2.3. TriGlobal instability analysis: three-dimensional LNSE

Without any restriction to the base flow, it depends on the three spatial directions

$$\mathbf{Q} = [U, V, W, P]^{\mathrm{T}}(x, y, z), \tag{11}$$

and modal perturbations get the form

$$\mathbf{q}(x, y, z, t) = \hat{\mathbf{q}}(x, y, z) \exp[-\omega t], \tag{12}$$

using the redefinition $\mathrm{i}\omega \to \omega$ in order to deal with a real problem.

Upon substitution of Eq. (12) into the LNSE, the operators $\mathcal{A}$ and $\mathcal{B}$ of Eq. (4) define a PDE-based problem in real arithmetic:

$$\mathcal{A}_{3D} = \begin{pmatrix} \mathcal{L}_{3D}+U_x & U_y & U_z & \mathcal{D}_x \\ V_x & \mathcal{L}_{3D}+V_y & V_z & \mathcal{D}_y \\ W_x & W_y & \mathcal{L}_{3D}+W_z & \mathcal{D}_z \\ \mathcal{D}_x & \mathcal{D}_y & \mathcal{D}_z & 0 \end{pmatrix}, \quad \mathcal{B}_{3D} = \begin{pmatrix} 1 & 0 & 0 & 0 \\ 0 & 1 & 0 & 0 \\ 0 & 0 & 1 & 0 \\ 0 & 0 & 0 & 0 \end{pmatrix}, \tag{13}$$

where $\mathcal{L}_{3D} = U\mathcal{D}_x + V\mathcal{D}_y + W\mathcal{D}_z - \frac{1}{Re}(\mathcal{D}_{xx} + \mathcal{D}_{yy} + \mathcal{D}_{zz})$, $\mathcal{D}_z$ being the first derivative matrix and $\mathcal{D}_{zz}$ the second derivative matrix respect to z direction.

2.4. The multidimensional Helmholtz eigenvalue problem

Turning to the main theme of the paper, solution of multidimensional eigenvalue problems arising in global flow instability, attention will be paid to the accurate recovery of analytically known results of the Poisson operator, the Helmholtz eigenvalue problem, which is at the heart of the elliptic part of the linearized Navier–Stokes equations governing instability in both two and three spatial dimensions:

$$\Delta\phi + \lambda^2\phi = 0, \tag{14}$$

where λ^2 is the sought real eigenvalue and can be determined analytically for simple geometries [34]. This problem is also recovered by simplification from the linearized Euler equations, neglecting flow velocity altogether and keeping only the pressure.

2.5. Boundary conditions

The elliptic eigenvalue problem (4) must be complemented with adequate boundary conditions for the disturbance variables. In the presence of solid walls, no-slip condition is implemented, and far from the wall all disturbances decay to zero. Boundary conditions for the disturbance pressure do not exist physically; instead on the boundaries, compatibility conditions are used derived from the Navier–Stokes equations at the boundary of the domain (see [35]).

3. Numerical methods and eigenvalue computation for matrix formation

In this Section the different spatial discretization methods for matrix formation used to solve global instability problems are presented. The eigenvalue computation to solve these problems is described in order to clarify the computational process followed in this paper.

3.1. Spatial discretization

The spatial discretization plays a very important role in matrix storing and forming approach for solving eigenvalue problems. In this Subsection different accurate numerical methods for matrix formation approach are briefly described. Special attention is devoted to the new high order finite difference methods developed by Hermanns and Hernández [32], since it is employed here for the first time in the global instability field.

3.1.1. Dispersion-relation-preserving finite difference schemes

The main objective of Dispersion Relation Preserving (DRP) finite difference schemes is to present an optimized high order finite difference scheme which minimizes dispersion wave errors. Therefore, this scheme supports not only consistency, stability and con-

vergence but also wave solutions with the same characteristics as the linearized Euler equations in the case of small amplitude waves. The methodology is briefly introduced in this paper and is explained more in detail by Tam and Webb in [29].

Considering the model wave equation

$$\frac{\partial u}{\partial t} = c\frac{\partial u}{\partial x}, \tag{15}$$

and using the spatial discretization on a uniform grid spacing Δx, the next expression gives the first order spatial derivative at the nodal point l:

$$\left(\frac{\partial u}{\partial x}\right)_l \simeq \frac{1}{\Delta x}\sum_{j=-N}^{M} a_j u_{l+j}, \tag{16}$$

where the finite difference coefficients a_j need to be determined. Additionally to the fulfillment of the classical finite difference relations among the coefficients a_j to ensure a certain order of convergence, the DRP methods impose conditions based on the minimization of the integrated error E, defined by the Euclidean norm,

$$E = \int_{-\pi/2}^{\pi/2} |\alpha\Delta x - \hat{\alpha}\Delta x|^2 \, d(\alpha\Delta x), \tag{17}$$

where α is the physical wavenumber and $\hat{\alpha}$ is the effective wave number of the finite difference approximation obtained from applying a spatial Fourier transformation to Eq. (16). This additional condition seeks to improve the spectral resolution capabilities of the explicit finite difference method [29].

The procedure to calculate second derivatives is similar to the one explained before. These coefficients are presented in Appendix A for a finite difference scheme of order 8.

Following the methodology employed in Merle et al. [36] the boundary formulation employed for the first and second derivative is a standard finite difference scheme. However, in this case the order of the boundary formulations are of the same order than the inner finite difference scheme. Such difference is necessary in order to get the proper slope of the relative error curves that preserve the order of the method.

3.1.2. Compact finite difference schemes

The implicit scheme or compact finite difference scheme described in [28] is briefly presented next. These schemes are generalizations of the Padé schemes. The considered mesh is again a regular one with a constant grid spacing Δx. The generalizations for the first and second derivatives have the following form:

$$\beta f'_{j-2} + \alpha f'_{j-1} + f'_j + \alpha f'_{j+1} + \beta f'_{j+2}$$

$$= c\frac{f_{j+3} - f_{j-3}}{6\Delta x} + b\frac{f_{j+2} - f_{j-2}}{4\Delta x} + a\frac{f_{j+1} - f_{j-1}}{2\Delta x}, \tag{18}$$

$$\beta f''_{j-2} + \alpha f''_{j-1} + f''_j + \alpha f''_{j+1} + \beta f''_{j+2}$$

$$= c\frac{f_{j+3} - 2f_j + f_{j-3}}{9\Delta x^2} + b\frac{f_{j+2} - 2f_j + f_{j-2}}{4\Delta x^2} + a\frac{f_{j+1} - 2f_j + f_{j-1}}{\Delta x^2}. \tag{19}$$

The coefficients employed to solve the system are presented in B and can be found in [28].

Following the methodology employed in [37] the boundary formulation employed for the first and second derivative is a finite difference compact scheme with smaller order than the inner scheme. However, in the present case the order of the boundary formulations are of the same order than the inner finite difference scheme. Such difference is necessary in order to get the proper slope of the relative error curves that preserves the order of the method.

3.1.3. Summation-by-Parts operators for finite difference approximations

Summation-by-Parts (SBP) operators can be used to construct time-stable high-order accurate finite-difference schemes as a discretization of the integration by parts formula. In this paper the basic idea of method construction is presented, which is explained more in detail in [30,31,38].

Considering the hyperbolic scalar equation $u_t + u_x = 0$, integration by parts can be expressed as

$$\frac{d}{dt}\|u\|^2 = -(u, u_x) - (u_x, u) = -u^2|_b^a, \tag{20}$$

where (u, v) is the standard L^2 inner product on $[a, b]$ and $\|u\|^2 = (u, u)$ is the associated L^2 norm. Considering the approximation of the equation $v_t + \mathcal{D}_x v = 0$, being v the discrete counter part of u, a difference operator $\mathcal{D}_x = H^{-1}Q$ is an SBP operator if $Q + Q^{\mathsf{T}} = B$, where $B = diag(-1, 0, \ldots, 0, 1)$. The procedure to calculate second derivatives is following as well a discretization of the integration by parts formula similar to the one explained before. The coefficients employed to perform first and second derivative for a finite difference scheme of order 8 can be found in [31].

3.1.4. Finite difference methods with uniform error, FD-q

The here called FD-q method developed by Hermanns and Hernández [32] is a new high order finite difference method employed to solve global instability problems for the first time in this paper. Therefore, more attention is paid in the description of this numerical method. The idea behind FD-q is to construct a non-uniform finite difference scheme based on the philosophy behind Chebyshev Gauss–Lobatto collocation points which minimize interpolation errors.

The approach followed for the derivation of the finite difference approximations is briefly presented in the following section. See the work by Hermanns and Hernández [32] for in-depth details of the presented method as well as its application to time evolution problems.

In order to derive the finite difference approximations to the spatial derivatives of a general function $u(x, t)$, a piecewise polynomial interpolant is constructed that matches the discrete values $u_i(t)$ of the function $u(x, t)$ at the grid nodes x_i, and whose derivatives are then computed to obtain the sought finite difference formulas. Fig. 1 represents such a piecewise polynomial interpolant formed out of individual polynomial interpolants $I_i(x)$ which are only valid in their respective domains of validity Ω_i. Each of these domains Ω_i includes the corresponding grid node x_i and their union is equal to the whole domain $[-1, +1]$ of the problem.

Given a set of grid nodes, the expressions for $I_i(x)$ can readily be obtained through the Lagrange interpolation formulae [39,40]:

$$I_i(x) = \sum_{j=s_i}^{s_i+q} \ell_{ij}(x)u_j, \qquad \ell_{ij}(x) = \prod_{\substack{m=0 \\ s_i+m\neq j}}^{q} \frac{x - x_{s_i+m}}{x_j - x_{s_i+m}}. \tag{21}$$

where q is the polynomial degree and the seed s_i is the index of the left most node x_i involved in the construction of the interpolant $I_i(x)$. For the case of even polynomial degrees, which is the choice from now on, the following selection of values for s_i is made:

$$\{s_i\} = \{\underbrace{0, \ldots, 0}_{q/2 \text{ times}}, \underbrace{0, 1, \ldots, N-q}_{\text{centered FD}}, \underbrace{N-q, \ldots, N-q}_{q/2 \text{ times}}\}. \tag{22}$$

The piecewise polynomial interpolant represented in Fig. 1 corresponds to the case of $q = 6$ and $N = 10$. As can be seen from the represented stencils of the individual interpolants, sufficiently far away from the boundaries, the above selection of seeds leads to centered finite difference formulas, whereas close to the boundaries
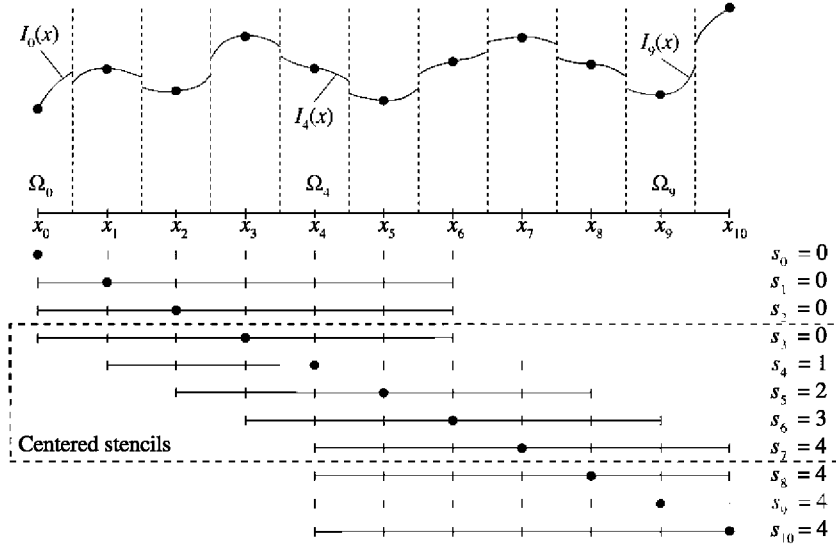
Fig. 1. Stencils, seeds s_i, and domains of validity Ω_i of the individual polynomial interpolants $I_i(x)$ of a piecewise polynomial interpolation of degree $q = 6$ on 11 nodes ($N = 10$). The dashed box separates the centered stencils from those affected by the presence of the boundaries.

the stencils are biased towards the center of the domain in order to only make use of existing grid nodes.

It should be noted, that in virtue of the uniqueness of the interpolating polynomials, the finite difference formulas obtained from the differentiation of the piecewise polynomial interpolant introduced above coincide with the ones obtained by classical means. Thus, no differences compared to conventional finite difference methods on arbitrary grids exist, only the way in which they are formulated and derived, but not in the end result.

In the above definition of the piecewise polynomial interpolant the choice of grid nodes x_i has been left open so far. However, by their proper selection it is possible to make the interpolation error of the piecewise polynomial interpolant to be uniform across the interval $[-1, +1]$. The result is a non-uniform grid that is unique for each pair of values of q and N. This same idea underlies the Chebyshev interpolation, where the condition that the interpolation error is uniform across the interval $[-1, +1]$ is also imposed, but this time on a single polynomial interpolant instead [41,42]. The result is also a non-uniform grid, known as the Chebyshev roots or Chebyshev-Gauss quadrature points, that is unique for each value of N. Both approaches achieve the same result, namely the suppression of the Runge phenomenon that spoils the accuracy of high order polynomial interpolations close to the ends of the interpolation interval.

In Fig. 2 the resulting grid spacings $\Delta x_i = x_{i+1} - x_i$ for the piecewise polynomial interpolant and for the Chebyshev interpolant are shown for different cases, both of them normalized with the uniform grid spacing $\Delta x_{i,Eq} = 2/N$. The details of the algorithm for the derivation of the former one can be found in [32], while the derivation of the Chebyshev grids can be found in any classical textbook on spectral collocation methods or interpolation theory [40–42]. The case $q = 6$ and $N = 10$ from Fig. 1 is shown in Fig. 2(a), where it can be seen that the proposed non-uniform grid for the piecewise polynomial interpolant lies in between the uniform grid and the Chebyshev grid.

Very enlightening are the following limiting cases: (i) $q \ll N$ and (ii) $q = N$. In the first case, only a few points $\mathcal{O}(q)$ close to the boundaries need to be clustered in order to control the interpolation error, while far from the boundaries the grid points are equally spaced, as seen in Fig. 2(b), where the case of a piecewise polynomial interpolant for $q = 6$ and $N = 30$ is shown. In the sec-

ond case, when $q = N$, only one interpolating polynomial can be constructed out of the $N + 1$ grid nodes, thus $I_0(x) = I_1(x) = \cdots = I_N(x)$. Due to the uniqueness of the interpolating polynomials and the fact that the same error uniformization strategy is used for the piecewise polynomial interpolant than for the Chebyshev interpolant, both approaches are identical. Thus, in the limit $q = N$, the proposed piecewise polynomial interpolant with the proposed non-uniform grid presents all the properties of spectral collocation methods, especially their spectral accuracy [42–44].

When $q < N$, most of the nodes are affected by the presence of the boundaries and the resulting grid point distributions are in between the two limiting cases. This can be seen in Fig. 2(c), where the grid spacing of the proposed non-uniform grids for different values of q and $N = 50$ are shown. As the degree of the interpolation increases, the node distribution approaches the Chebyshev grid, while for small values of q it is more close to the uniform grid. Fig. 2(d) shows that the minimum grid spacing Δx_{min} present in the proposed non-uniform grids is always greater than the minimum grid spacing $\Delta x_{min,Ch}$ of the Chebyshev grid. Moreover, from the figure in can be inferred that $\Delta x_{min} = \mathcal{O}(\Delta x_{min,Ch} N/q) = \mathcal{O}((qN)^{-1})$.

3.1.5. Spectral collocation methods

The limit of $q = N$ in the FD-q methodology is the Chebyshev-Gauss–Lobatto spectral collocation method. The spectral methods offer an optimal compromise between the highest accuracy possible and the necessity of reducing the amount of information to be stored. The reason of the high accuracy of (collocation) spectral methods lies in the use of high-order interpolating polynomials, comprising all the points in the discretization domain. Spectral methods use all the points and the error is $\varepsilon = \mathcal{O}((1/N)^N) \rightarrow \mathcal{O}(e^{-N})$ [42,43]. Chebyshev-Gauss–Lobatto (CGL) points:

$$x_j = \cos(j\pi/N), \quad j = 0, 1, \ldots, N, \tag{23}$$

indicated for the non-periodic configurations of interest, are used here. It is important to note again that these points are equivalent to the points obtained by using FD-qN and the elements of the differentiation matrix $\mathcal{D}$ depend solely on the set of discretization points. Derivative matrices are defined in [43,42].
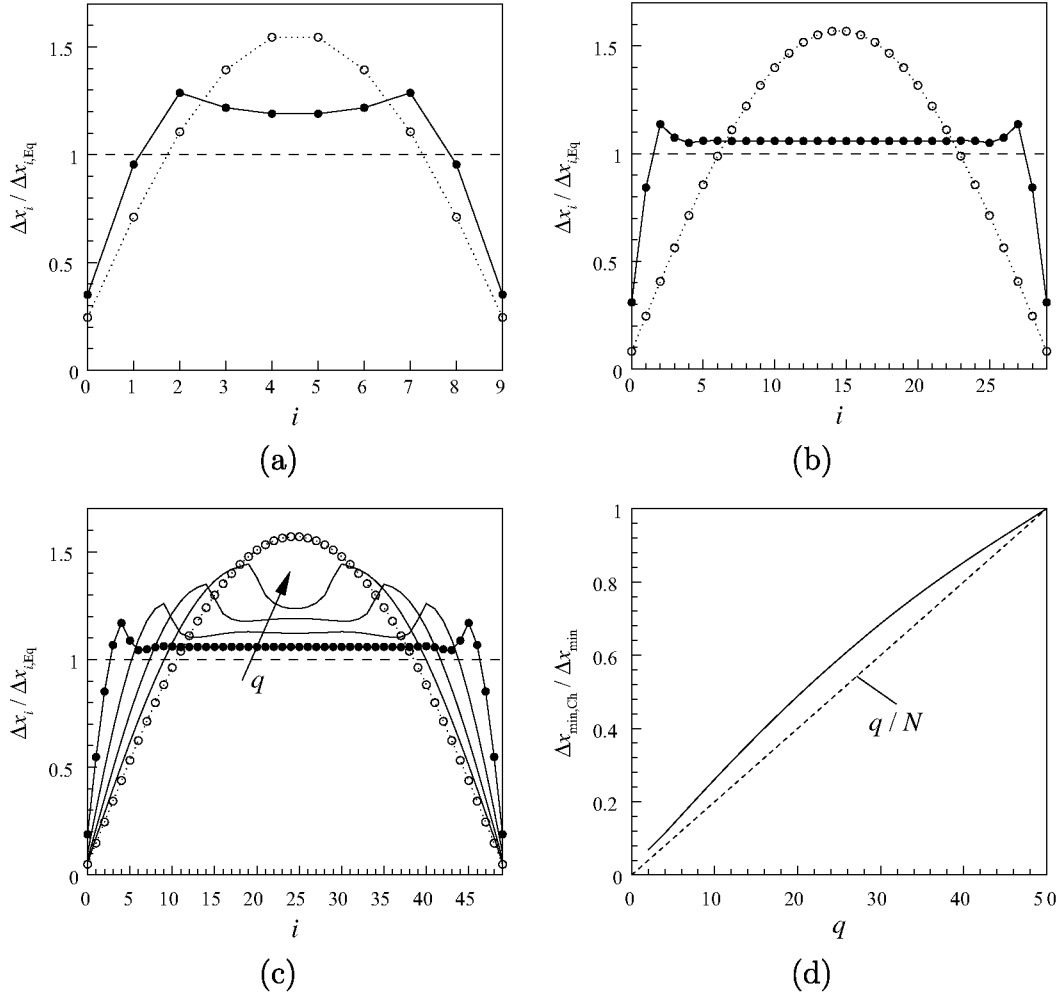
Fig. 2. Grid spacing $\Delta x_i = x_{i+1} - x_i$ of the non-uniform grid for the piecewise polynomial interpolation (solid line), for the Chebyshev interpolation (dotted line), and for the uniform grid (dashed line) normalized with the uniform grid spacing $\Delta x_{i,Eq} = 2/N$ for (a) $q = 6$ and $N = 10$, (b) $q = 6$ and $N = 30$, and (c) $q = 10, 20, 30, 40$ and $N = 50$. (d) Variation of $\Delta x_{min,Ch}/\Delta x_{min}$ with q of the non-uniform grid for the piecewise polynomial interpolation with $N = 50$.

3.2. Eigenvalue computation

The generalized eigenvalue problems must be constructed and solved employing adequate algorithms, taking into account the memory and CPU-time requirements when the matrices are formed and stored. Although the algorithm allows for the use of dense or sparse linear algebra, the sparse version is much more efficient and it is the one used here. The complex matrices $\mathcal{A}$ and $\mathcal{B}$ of Eq. (4) are built using an in-house modified version of the SPARSKIT2 library [45] to work with complex arithmetic. To solve the eigenvalue problem, the Arnoldi algorithm [46] is employed, combined with the MUMPS library [47,48] (MUltifrontal Massively Parallel Solver) to perform the LU-decomposition and solve the linear algebraic systems with the possibility of making serial and parallel computations.

The Arnoldi algorithm delivers a number of eigenvalues on the vicinity of a specific estimate value. Such value is set in the vicinity of the unstable/least-stable eigenvalue. Computational cost is greatly reduced when employing Arnoldi algorithm instead of the classical QZ method. More details can be found in the literature [46,21].

4. Results on the eigenvalue problem

In a linear modal framework, the overall behaviour of an unstable dynamical system is determined by its leading unstable eigenvalues. Owing to the exponential growth of potential inaccuracies in the eigenvalues, the major concern when performing fluid flow instability analyses is to capture in an accurate manner both the real and the imaginary parts of, at least, the leading eigenmodes. This statement is true independently of the dimensionality of the base flow; however, on account of ambiguities in the base state determination, few global linear instability analyses are available with sufficient quality to be used for validation of those delivered by the spatial discretizations proposed herein.

In this respect, validations commence with the well-known Orr-Sommerfeld equation (OSE), to which the global eigenvalue problem reduces in case of parallel flows. Results are presented for the plane Poiseuille flow (PPF) [49,50] and for the Blasius boundary layer [51].

Eigenvalue problems whose spatial dependence is described by the Poisson operator are subsequently solved by the present methodology, in both two and three spatial dimensions. The attractiveness of this spatial operator resides in the existence of analytically-known results in regular two- and three-dimensional geometries and also in the fact that this spatial operator is at the heart of the global eigenvalue problem in both two and three spatial dimensions.

In the main topic of this paper, global modal instability analysis results are obtained in five fluid flow applications, three in a BiGlobal and two in a TriGlobal eigenvalue problem context. The BiGlobal eigenvalue problems to solve differ in the number of base

flow components: in the rectangular duct [6] only one such component exists, and the EVP is complex; in the 2D lid-driven cavity [52], two base flow velocity components exist, while the wavenumber vector is normal to the base flow plane, and the stability eigenvalue problem is real; in the swept attachment-line boundary layer [53] all three base flow components exist and the eigenvalue problem is again complex. Finally, TriGlobal linear instability eigenvalue problems are solved, treating all three inhomogeneous spatial dimensions in a coupled manner. This is the most stringent test to which the proposed spatial discretization is employed. The same rectangular duct and 2D lid-driven cavity problems studied by BiGlobal analysis are solved by TriGlobal analysis. The solution is obtained at length-to-depth ratio of unity and a spanwise domain extent defined by the maximally amplified BiGlobal eigenmode, with which the TriGlobal analysis results are compared. It is worth noting that the very first TriGlobal instability analysis to appear in the literature was performed relatively recently in a time-stepping context [18], while presently four more such analyses are available [54,19,55,56]. Of these, one [54] is performed in a matrix-forming context, while two in a time-stepping technique, all concerning the cubic lid-driven cavity with singular lid motion [55,56].

4.1. Local instability analysis

The one-dimensional LNSE is the limit to which the global eigenvalue problem reduces in case of parallel flows. Results are presented for the plane Poiseuille flow (PPF) [49,50], the bounded nature of which implies the existence of a discrete eigenspectrum only, and for the Blasius boundary layer [51], where both discrete and continuous branches of the spectrum exist.

In order to assess the ability of the proposed spatial discretization to perform transient growth studies, the well-known pseudo-spectra of the OSE [57] are also obtained.

4.1.1. Eigenspectrum of plane Poiseuille flow

The temporal stability analysis of the plane Poiseuille flow is considered first. The stability eigenvalue problem [49] is solved at $Re = 10000, \alpha = 1$ and spanwise wavenumber $\beta = 0$, for which the converged leading eigenvalue in double precision arithmetic has been provided by Kirchner [58] as being $\omega_{r,c} + i\omega_{i,c} = 0.2375264888204682 + i0.0037396706229799$. Owing to the relatively small leading matrix dimension, the dense linear algebra subroutine ZGGEV of LAPACK, based on the QZ algorithm [59], is used for the solution of the eigenvalue problem. The examined spatial discretizations are summarized in Table 1. All these finite difference methods are implemented at order 8 and on uniform grids, except for the last one, FD-q, which employs its particular grid. In addition, FD-q method is implemented not only at order 8, but also at order 16, in order to prove the capability of this method of reaching the resolution properties of very high order schemes. In Fig. 3, relative error of the leading eigenvalue as function of the leading matrix dimension $N + 1$ is presented in order to compare accuracy between the different numerical methods. The relative error is defined in the following way:

Table 1
Examined spatial discretization methods.

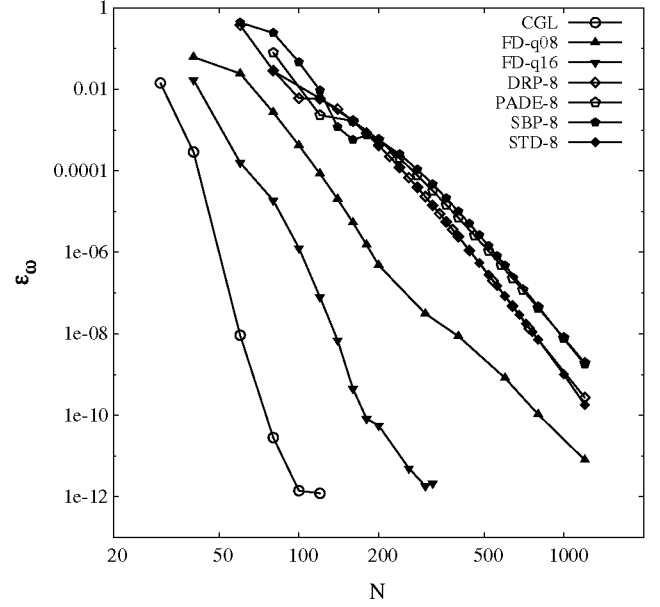| Spatial discretization method	Acronym	References
Spectral collocation	CGL	[43,42]
Standard centered finite differences	STD	–
Compact finite-differences	Padé	[28]
Dispersion-Relation-Preserving finite differences	DRP	[29]
Summation-by-parts operators	SPB	[30,31]
Finite difference methods with uniform error	FD-q	[32]

Fig. 3. Relative error for the amplification rate of the leading eigenmode of plane Poiseuille flow at $Re = 10^4, \alpha = 1$ [49,50], obtained by (black) spectral collocation using CGL and (blue) high-order finite-difference methods of order 8: STD, Padé, DRP, SBP, as well as (red) FD-q with $q = 8$ and $q = 16$. $N + 1$ is the total number of discretization points. (For interpretation of the references to colour in this figure legend, the reader is referred to the web version of this article.)

$$\varepsilon_\omega = \left| \frac{\omega_i - \omega_{i,c}}{\omega_{i,c}} \right|, \tag{24}$$

where ω_i is the computed imaginary part of the eigenvalue using $N + 1$ nodes and $\omega_{i,c}$ the corresponding converged value quoted above.

Several observations are worthy of discussion on the basis of these results and the analogous ones of the mode frequency, as well as all qualitatively identical results obtained for FD-q at different combinations of discretization nodes, $N + 1$, and orders, q, not presented here. First, it is seen that, compared with any finite-difference method, the spectral collocation method needs less grid points to obtain a converged result, a fact which is well-known from classic linear stability studies [e.g. 60]. Second, when monitoring finite-difference discretizations of the same order (here methods of order 8 are shown), the standard and the compact finite-differences, the DRP and the SBP methods all require practically the same resolutions in order to deliver amplification rate results converged to the same degree. However, fastest convergence, compared with any of the examined finite-difference methods of the same order, is offered by the FD-q8 method. In the example presented, in order to achieve a relative error of $\mathcal{O}(10^{-6})$ in the amplification rate, $N \approx 200$ points are needed by FD-q8 and $N \approx 500$ by all other finite-difference methods despite having all of them the same formal order of accuracy/convergence. Conversely, and much more important from the point of view of the subsequent use of the FD-q methods as the basis for spatial discretization in the multi-dimensional eigenvalue problems, at a given affordable level of discretization, say $N = 200$ points, STD, Padé, SBP and DRP methods of order 8 have a relative error of $\mathcal{O}(10^{-3})$ in the recovery of the leading eigenmode, while the error of the FD-q8 method is $\mathcal{O}(10^{-6})$. Third, as the order of the FD-q method is increased, its results approach those of the spectral collocation method, with which the method becomes identical when $q = N$ as discussed in Section 3.1.4; the FD-q16 results shown in Fig. 3 are typical for the convergence history shown by FD-q methods of order $8 < q < N$, requiring only $N \approx 100$ points to achieve the

specified relative error level of $\mathcal{O}(10^{-6})$, or attaining an accuracy of $\mathcal{O}(10^{-10})$ for $N = 200$ points.

In summary, at all orders examined, the FD-q method performs better than all of the well-known high-order finite-difference methods. This is attributed to the fact that the FD-q method minimizes the interpolation error both at the interior and the boundary (and near-boundary) points in a self-consistent uniform manner. In order for the standard high-order, Padé, DRP or SBP schemes to become competitive with FD-q, higher formal orders need to be used compared with that employed in the FD-q method. However, that increase in the order may not be straightforward for some schemes at $q \geqslant 8$ [30] or the resulting finite difference method may be unstable.

On the other hand, for those methods for which using $q > 8$ is possible, the increase in bandwidth resulting from a comparatively high value of q is not an issue from the point of view of efficiency, when the one-dimensional eigenvalue problem is solved using full eigenspectrum computations and the QZ algorithm. However, FD-q has a competitive advantage in performing global instability analyses, where exploitation of the matrix sparsity is essential; there one seeks to use the method having optimal convergence and accuracy properties between all available having the same sparsity pattern, as will be discussed in subsequent sections.

4.1.2. Pseudospectrum of plane Poiseuille flow

The non-modal scenario for laminar-turbulent flow transition is now well-understood [33], the concept of pseudospectrum [61] being central to its theoretical description. In this Subsection the pseudospectrum of plane Poiseuille flow (PPF) is shown comparing, for brevity, Chebyshev-Gauss–Lobatto collocation (CGL) and FD-q16.

As in the previous Section, results obtained are representative of all combinations of number of discretization points, N, and finite-difference method order, q for FD-q; $N = 128$ and $q = 16$ are used presently, and the pseudospectrum has been computed using Eig-Tool [62].

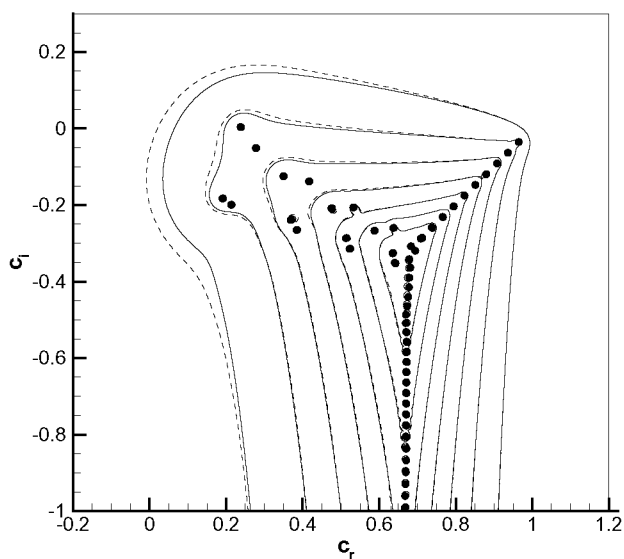Fig. 4 shows the eigenspectrum and pseudospectrum obtained by the spectral collocation and finite-difference methods.

Eigenspectrum results are graphically indistinguishable from each other while the pseudospectrum, plotted here at different levels of matrix perturbations, corresponding to 10^{-7} for the innermost to 10^{-2} in the outermost curve in Fig. 4, only shows discrepancies at large matrix perturbation levels. However, given that $q \ll N$, the overall agreement is quite satisfactory. If an improved agreement is sought, the order q or the number of points N may be increased in order for the FD-q method to deliver results approaching those obtained by the spectral collocation method. As mentioned, though, it is not perfect agreement of the FD-q with the spectral collocation method that is sought, but rather the ability of the former method to deliver accurate description of the pseudospectrum, as shown in the results of Fig. 4, at a smaller cost thanks to the fact that $q \ll N$, thus improving the sparsity pattern.

4.1.3. Eigenspectrum of the Blasius boundary layer

The accuracy properties of the FD-q method are preserved in open flows, where a mapping transformation is needed to transfer data from the standard domain $x \in [-1, 1]$ of both the CGL and the FD-q methods onto a semi-infinite domain $y \in [0, y_\infty]$. The transformation used is

$$y = L\frac{1 - x}{1 + s + x}, \quad L = \frac{y_\infty y_{\frac{1}{2}}}{y_\infty - 2y_{\frac{1}{2}}}, \quad s = 2L/y_\infty, \tag{25}$$

where $y_\infty = 150$ is the location where the calculation domain is truncated, with half the points being placed between the wall and $y_{\frac{1}{2}} = 5$ [60].

Fig. 5 shows the leading unstable eigenmode and the least stable part of the Blasius eigenspectrum at $Re_{\delta^*} = 580$ and $\alpha = 0.179$ [51], as recovered by the CGL spectral collocation method on $N + 1 = 101$ points, as well as FD-q12 and FD-q24 on the same number of nodes. Even at a value of q which is an order of magnitude smaller than N, the entire discrete eigenspectrum is seen to be recovered by the FD-q method as reliably as by the CGL spatial discretization. None of the three methods is capable of capturing the continuous spectrum correctly; as is known analytically, the latter
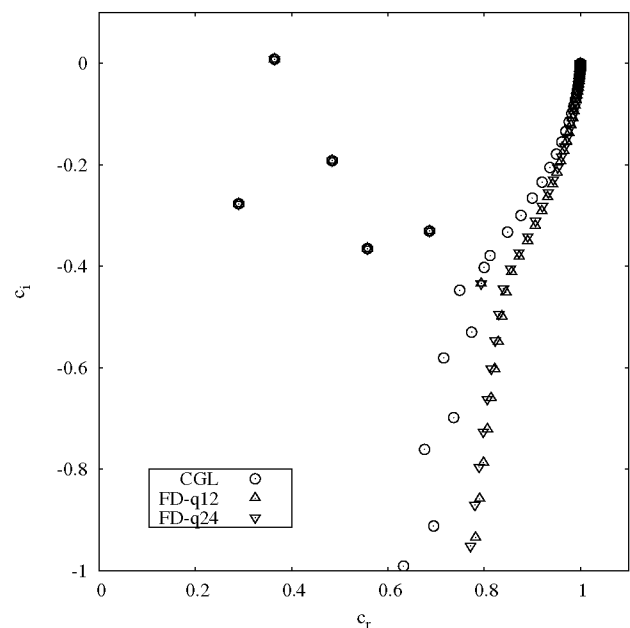

Fig. 4. Eigenspectrum and pseudospectrum of plane Poiseuille flow at $Re = 10^4, \alpha = 1$ [49], obtained by spectral collocation using CGL and high-order finite-difference method FD-q. Solid lines and empty circles: CGL, Dashed lines and solid circles: FD-q16, both of them with $N + 1 = 129$ discretization points. Levels from inner to outer isoline, $10^{-7}, 10^{-6}, 10^{-5}, 10^{-4}, 10^{-3}, 10^{-2}$. Note that $c = \omega/\alpha$ refers to phase velocity.

Fig. 5. Eigenspectrum of Blasius flow at $Re_{\delta^*} = 580$ and $\alpha = 0.179$ [51], obtained with spectral collocation based on mapped CGL and two high-order finite-difference methods FD-q of order 12 and 24 with $N + 1 = 101$ discretization points. Note that $c = \omega/\alpha$ refers to phase velocity.

is a vertical line at $c_r = \omega_r/\alpha = 1$ (c refers to phase velocity). Interestingly, even at $q = 12$ the discrete approximation of the continuous spectrum is more vertical than the one delivered by the spectral collocation method, although as q increases the FD-q and spectral results come closer, and collapse onto each other at $q = N$, pointing towards the existence of an optimum value of q which is unknown a priori. Finally, an additional discrete mode is recovered at $c_r = 0.8$ using the FD-q12 and FD-q24 methods due to the displacement of the continuous part of the spectrum.

4.1.4. Pseudospectrum of the Blasius boundary layer

This Subsection of validation of results of the FD-q method against known solutions of the one-dimensional eigenvalue problem closes with the presentation of the pseudospectrum of Blasius flow at the same parameters as those at which the eigenspectrum has been obtained. Fig. 6 presents the eigenspectrum obtained by the spectral collocation method, already shown in Fig. 5, alongside the one delivered by FD-q16, which exhibits the properties discussed in the previous Subsection. In addition, the pseudospectrum obtained at perturbation levels of 10^{-7} to 10^{-2} (inner-to-outer curves) is shown. As in the case of the plane Poiseuille flow, close qualitative agreement is seen between the two sets of results, although the poor recovery of the continuous spectrum by both, the spectral and the finite-difference methods, results in larger discrepancies in the pseudospectrum in that region. By contrast, the pseudospectrum associated with the discrete eigenvalues is reproduced in close agreement by both methods, despite the fact that $q = 16$ is an order of magnitude smaller than $N + 1 = 129$, the discretization nodes used in both methods.

4.2. The 2D Helmholtz eigenvalue problem

In two spatial dimensions the Helmholtz eigenvalue problem (14) is:

$$\left(\frac{\partial^2}{\partial x^2} + \frac{\partial^2}{\partial y^2}\right)\phi + \lambda^2\phi = 0. \tag{26}$$

Such problem is useful in assessing the accuracy of the proposed spatial discretization method comparing the recovered eigenvalues with the analytical solution of this problem in the rectangular membrane domain $\Omega = \{x \in [-1,1]\} \times \{y \in [-1,1]\}$ [e.g. 34]. Such solution is the following:

$$\lambda^2_{n_x,n_y} = \frac{\pi^2}{4}(n_x^2 + n_y^2); \quad n_x, n_y = 1, 2, 3, \ldots \tag{27}$$

Higher eigenvalues/eigenfunctions ($n_x, n_y \gg 1$) are of special interest due to the need of using a relatively high number of nodes for an accurate description. This is in contrast with the first few eigenvalues, which are already recovered using $N \approx 10$.

Fig. 7 shows the convergence history of the numerical solution of the 2D Helmholtz problem for a high eigenvalue ($\lambda^2/(\pi^2/4) = 34$) comparing the same finite difference methods used to obtain the OSE results in Fig. 3. Similar conclusions to the one reached in the Orr-Sommerfeld flow instability problem solved in the previous applications are also drawn here: maintaining the order of the scheme (order 8) FD-q presents higher accuracy than the other finite difference methods, and with a higher order (order 16), FD-q reaches double-precision employing a number of nodes only two times larger than employing the spectral collocation method.

Fig. 8(a) shows the convergence history of the numerical solution of the 2D Helmholtz problem for the same eigenvalue. Different orders of FD-q methods are implemented and compared with CGL spectral collocation method. Special interest is focused on intermediate values of the order of the method, e.g. $q = 12$. In such case single-precision convergence is achieved using approximately two times more discretization points than with the spectral collocation method. In addition, double-precision convergence is achieved with less than four times more nodes than the ones required by the spectral collocation method. For completeness,
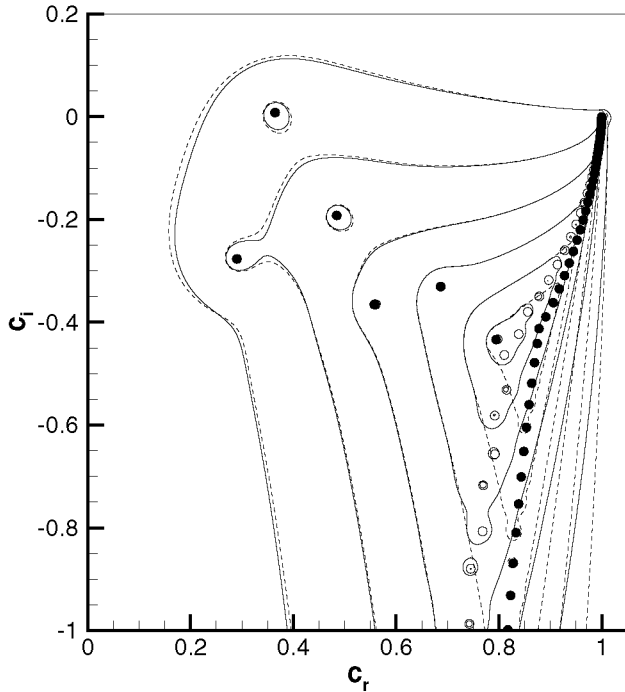

Fig. 6. Eigenspectrum and pseudospectrum of the Blasius boundary layer at $Re_{\delta^*} = 580$ and $\alpha = 0.179$ [51], obtained by spectral collocation using CGL and FD-q. Solid lines and empty circles: CGL, Dashed lines and solid circles: FD-q16, both of them with $N + 1 = 129$ discretization points. Levels from inner to outer isoline, $10^{-7}, 10^{-6}, 10^{-5}, 10^{-4}, 10^{-3}, 10^{-2}$.
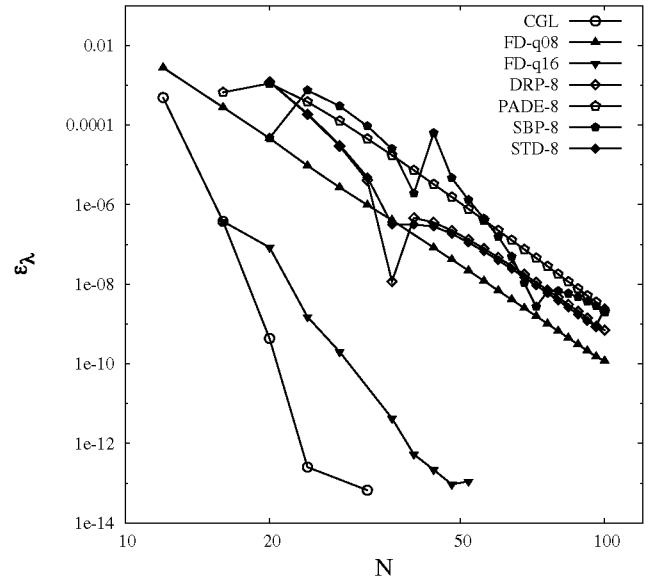

Fig. 7. Convergence history of the solution of the 2D Helmholtz eigenvalue problem for the eigenvalue $\lambda^2/(\pi^2/4) = 34$, obtained by (black) spectral collocation using CGL and (blue) high-order finite-difference methods of order 8: STD, Padé, DRP, SBP, as well as (red) FD-q with $q = 8$ and $q = 16$. The number of discretization nodes used is the same in both spatial directions and is denoted by $N + 1$. (For interpretation of the references to colour in this figure legend, the reader is referred to the web version of this article.)
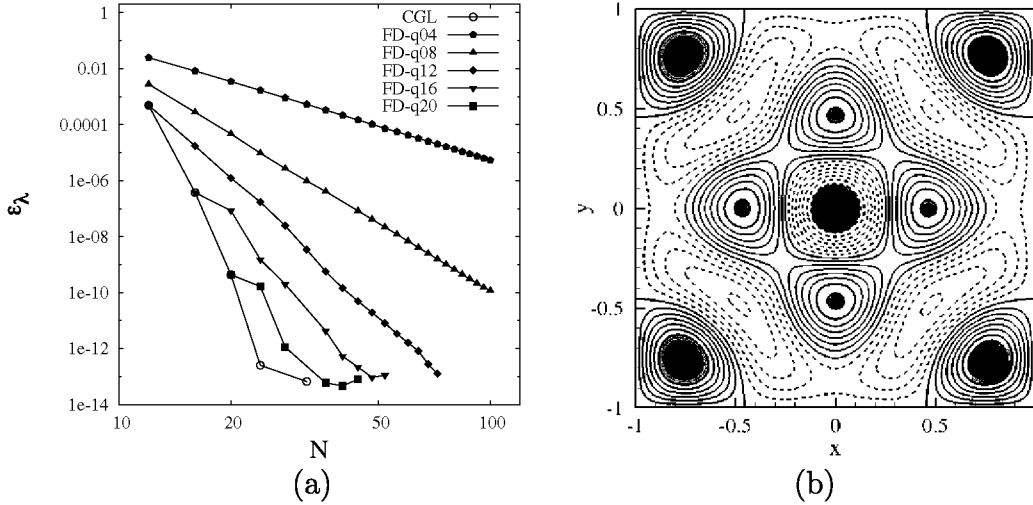
Fig. 8. (a) Convergence history of the solution of the 2D Helmholtz eigenvalue problem for the eigenvalue $\lambda^2/(\pi^2/4) = 34$, obtained using CGL and a suite of FD-q methods of orders 4, 8, 12, 16 and 20. The number of discretization nodes used is the same in both spatial directions and is denoted by $N + 1$. (b) Corresponding eigenfunction using FD-q12 with $N_x \times N_y = 80^2$. Shown are contours ($-0.9{:}0.1{:}0.8$) with isolines of positives (solid line) and negatives (dashed line) values.

Fig. 8(b) displays the eigenfunction corresponding to the eigenvalue $\lambda^2/(\pi^2/4) = 34$, obtained numerically using FD-q12 with $N_x \times N_y = 80^2$.

4.3. BiGlobal instability analysis

Attention is now turned to the main subject of this paper, namely modal global linear instability, discussing BiGlobal instability first. Three applications are selected for validation purposes: the rectangular duct [6], the lid-driven cavity [52,63] and the swept leading-edge boundary layer [53,64]. As mentioned in the introduction to this section, these problems are selected because they are governed by one, two and three base flow velocity components, respectively, and also permit validating both the real and the complex form of the eigenvalue problem.

4.3.1. The rectangular duct flow

In two coupled spatial directions, the rectangular duct [6] of cross-sectional aspect ratio A, driven by a constant pressure gradient along the axial (unbounded) direction, is the two-dimensional extension of the plane Poiseuille flow. Its base flow is known analytically [65] and has a single component along the (homogeneous) wavenumber vector direction. Global flow instability in this application is governed by a complex eigenvalue problem.

Considering the rectangular duct defined in the domain $\Omega = \{x \in [-A,A]\} \times \{y \in [-1,1]\}$, a constant pressure gradient in the unbounded z direction drives a steady laminar flow which is independent of z and possesses a velocity vector $\mathbf{U} = [0,0,W(x,y)]^\mathsf{T}$ with a single velocity component $W(x,y)$ along the z spatial direction. The latter satisfies the Poisson equation that may be solved in series form [66].

Table 2 presents convergence history results for the numerical solution of the 2D EVP presented in Eq. (4) using the matrices (10) with base flow velocity $\mathbf{U} = [0,0,W(x,y)]^\mathsf{T}$, using CGL and FD-q16 at a subcritical Reynolds number, $Re = 1000$, and wavenumber parameter $\beta = \pi$. In addition, Richardson-extrapolation results are also shown. Considering the Richardson extrapolation value of CGL spectral collocation method as converged eigenvalue, 8 decimal digits are converged in ω_r and 9 in ω_i when using CGL methods with $N^2 \geqslant 60^2$. On the other hand, the same order of convergence is reached when using FD-q16 with $N^2 \geqslant 90^2$. Fig. 9

Table 2
Convergence history of BiGlobal instability analysis of rectangular duct flow at $A = 1, Re = 1000$ and $\beta = \pi$ comparing the leading eigenmode results using CGL and FD-q16 and the corresponding Richardson extrapolations.

	N^2	ω_r	ω_i
CGL	30^2	2.9027647730	−0.10353535398
	40^2	2.9027654432	−0.10352492808
	50^2	2.9027654495	−0.10352492616
	60^2	2.9027654518	−0.10352492608
	70^2	2.9027654528	−0.10352492609
Richardson Ext.		2.9027654541	−0.10352492635
FD-q16	30^2	2.9027679758	−0.10352715467
	50^2	2.9027654409	−0.10352492446
	70^2	2.9027654496	−0.10352492422
	90^2	2.9027654520	−0.10352492512
	110^2	2.9027654529	−0.10352492555
Richardson Ext.		2.9027654541	-0.10352492637

shows the convergence history for the different spatial discretization schemes, using the converged result of Table 2, $\omega = 2.9027654541 - i0.10352492635$, as correct value. Different slopes arise due to the discontinuities of the derivatives in the corners of the domain [43]. As expected, the convergence rate for FD-q16 and CGL are better than for the order 8 schemes. However, the higher degree of sparsity in the 8th-order scheme makes FD-q8 the more efficient one in terms of the numerical solution of the 2D EVP presented in Eq. (4) with the matrices (10).

4.3.2. The regularized lid-driven cavity

The two-dimensional lid-driven cavity, three-dimensional (non-zero spanwise wavenumber) BiGlobal instability analysis of which was first performed using singular boundary conditions [52,63], is solved next, after regularizing the lid motion. Regularization eliminates the corner singularities at the two ends of the moving lid and permits obtaining highly-accurate base flow solutions. Regarding global instability in this problem, the wavenumber vector is normal to the plane on which the base flow develops, and a simple transformation of the linearized Navier–Stokes equations reduces the two-dimensional eigenvalue problem into one governed by real coefficients [21].
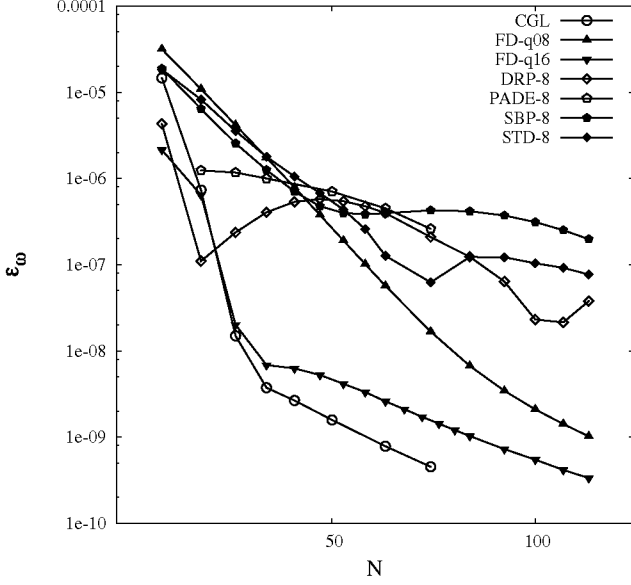
Fig. 9. Convergence history of the BiGlobal eigenvalue problem applied to the rectangular duct flow at $Re = 1000$ and $\beta = \pi$, with $A = 1$ for the eigenvalue $\omega = 2.9027654541 - i0.10352492635$, obtained by (balck) spectral collocation using CGL and (blue) high-order finite-difference methods of order 8: STD, Padé, DRP, SBP, as well as (red) FD-q with $q = 8$ and $q = 16$. The number of discretization nodes used is the same in both spatial directions and is denoted by $N + 1$. (For interpretation of the references to colour in this figure legend, the reader is referred to the web version of this article.)

Fig. 10. Convergence history of the BiGlobal eigenvalue problem applied to the regularized lid-driven cavity flow at $Re = 1000$ and $\beta = 15$, with $A = 1$ for the most unstable eigenvalue $\omega = i0.108337$, obtained by (black) spectral collocation using CGL grid and (blue) high-order finite-difference methods of order 8: STD, Padé, DRP, SBP, as well as (red) FD-q with $q = 8$ and $q = 16$. The number of discretization nodes used is the same in both spatial directions and is denoted by $N + 1$. (For interpretation of the references to colour in this figure legend, the reader is referred to the web version of this article.)

The direction x is taken to be in the direction of the motion of the lid and y to be along the normal to this direction. The base flow is considered independent of the third (spanwise) direction z. Thus, the domain is defined as $\Omega = \{x \in [0, A]\} \times \{y \in [0, 1]\}$, where A is the aspect ratio. The steady base flow vector under these assumptions has two velocity components, $\mathbf{U} = [U(x, y), V(x, y), 0]^T$, and it is obtained by solving the vorticity-transport equation (see [21] for more details). The boundary conditions are $V = 0$ on all four walls and $U = 0$ in all the walls but the corresponding to the lid where

$$U = \left[1 - (2x - 1)^{16}\right]^2, \quad x \in [0, 1]. \tag{28}$$

In this manner, the discontinuity in the boundary condition at $U(x = 0, y = 1)$ and $U(x = 1, y = 1)$ of the lid-driven-cavity flow [67,68] is avoided, since it is a potential source of suboptimal convergence.

Fig. 10 presents convergence history results using the same suite of 8th-order finite difference methods used so far, in addition to FD-q16 and CGL. At the conditions at which the eigenvalue problem in Eq. (4) with the matrices (10) is solved, the leading eigenmode is stationary, so comparisons are performed using only the imaginary part of the leading eigenvalue. The converged value used for this result is the average obtained while Richardson extrapolation of the CGL and FD-q16 methods. The same qualitative conclusions reached by application of these discretization methods in the previous problems are reached here too, namely that the FD-q methods are superior in terms of accuracy to all other finite-difference approaches.

It is worth noting in this context that the only previous known work in the literature which compares finite-difference and spectral collocation methods for global instability analysis is the work by Merle et al. [27] who also used the lid-driven cavity as test. The conclusion reached in that work was that the DRP scheme is the best alternative in terms of computational cost to CGL from a combined accuracy and efficiency perspective. This conclusion is
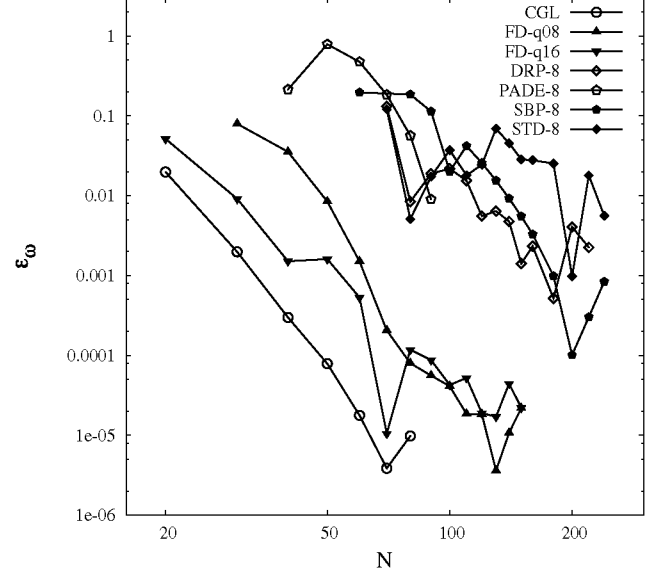
superseded by the results of Fig. 10: while the DRP method has the same formal resolution capacity as standard, Padé or SBP finite-differences, and may indeed be more efficient than some of the other methods examined (comparisons in [27] were confined to Padé and DRP), the 8th-order member of the FD-q methods family significantly outperforms all its peers; using $N = 100$ it delivers a relative error of the most unstable eigenmode of $\mathcal{O}(10^{-4})$, as opposed to $\mathcal{O}(10^{-2})$ that all other finite-difference methods deliver. In addition, due to the nature of the method, the sparsity of DRP is smaller than the one of FD-q when the order of the method is the same in both numerical schemes. As in the previously studied problems, increasing the order of the FD-q method utilized delivers results approximating those obtained by the spectral collocation method.

4.3.3. The swept attachment-line boundary layer flow

Still within a BiGlobal context, the eigenvalue problem governing instability of the incompressible swept Hiemenz flow is also solved using the proposed spatial discretization methods. Unlike the two previous two-dimensional base flows, here all three base flow velocity components are present and no reductions of the linearized Navier–Stokes equations are possible. Here too a complex eigenvalue problem needs to be solved. One advantage of this application is that the base flow is obtained by the solution of systems of coupled ordinary differential equations at arbitrarily high precision. In addition, accurate global instability results of this flow are available [53] and have been modeled by simple one-dimensional eigenvalue problems in both the orthogonal [64], and the non-orthogonal [69] leading-edge boundary layer flow, providing highly accurate data to compare against.

The base flow is provided by the swept Hiemenz boundary layer, which models steady stagnation line flow. The velocity components are independent of the homogeneous direction along the attachment line, z, which is assumed to be infinite, while all three base flow velocity components are taken to depend on the wall-normal direction y. Moreover, the chordwise velocity component

	N^2	$c_r(GH)$	$c_i(GH)(\times 10^2)$	$c_r(A1)$	$c_i(A1)(\times 10^2)$
CGL	30^2	0.35840506	0.58473709	0.35791126	0.41108252
	40^2	0.35841015	0.58531622	0.35792172	0.41104656
	50^2	0.35840978	0.58532857	0.35792622	0.41027206
	60^2	0.35840997	0.58531393	0.35792318	0.40962663
FD-q16	30^2	0.35842026	0.58484758	0.35792767	0.40974017
	50^2	0.35840951	0.58533098	0.35791855	0.40989817
	70^2	0.35840947	0.58529166	0.35791927	0.40986547
	90^2	0.35840990	0.58532679	0.35791979	0.40988838
FD-q8	30^2	0.35840088	0.58685134	0.35790972	0.41179370
	50^2	0.35841011	0.58540140	0.35797511	0.40990771
	70^2	0.35840976	0.58530175	0.35791916	0.40989455
	90^2	0.35840991	0.58532658	0.35791980	0.40988576
L&M [53]		0.35840982	0.58532472	0.35791970	0.40988667

$U(x, y)$ is taken to be linearly dependent on the chordwise coordinate x, while the wall-normal velocity component $V(y)$ and the velocity component $W(y)$ along the attachment line are taken to be independent of x [65].

The eigenvalue problem in Eq. (4) with the matrices (10) is solved with this attachment line boundary layer base flow using the same set of parameters of [53]: $Re = 800$ and $\beta = 0.255$. The transformation used for the wall-normal direction y is the same as the one used for the Blasius boundary layer problem (25) but with $y_\infty = 150$ and $y_{\frac{1}{2}} = 4$. In the chordwise coordinate, a linear transformation is used to map the standard CGL or FD-q domain into $x \in [-200, 200]$. Table 3 shows comparisons with the converged results of [53] using CGL, FD-q8 and FD-q16 for the first two most unstable modes. FD-q8 and FD-q16 results show very good agreement with the literature result and even outperform the CGL results of the second eigenvalue using low resolution (e.g. $N_x \times N_y = 50^2$), which is more difficult to be calculated numerically, due to the closeness between both modes.
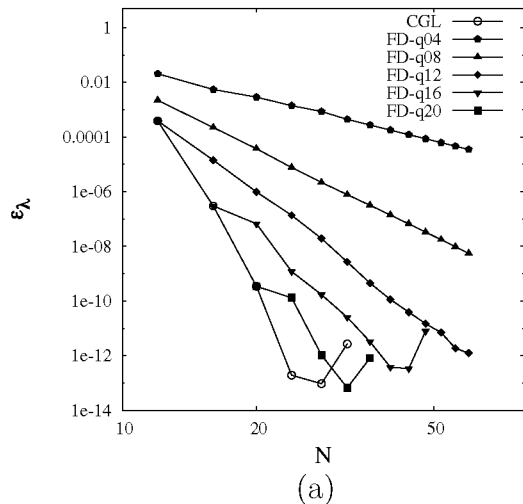
4.4. The 3D Helmholtz eigenvalue problem

In three spatial dimensions the Helmholtz eigenvalue problem (14) is defined by the following equation:

$$\left(\frac{\partial^2}{\partial x^2} + \frac{\partial^2}{\partial y^2} + \frac{\partial^2}{\partial z^2}\right)\phi + \lambda^2\phi = 0, \tag{29}$$

Such problem is useful in assessing the accuracy of the proposed spatial discretization method, especially in the recovery of the higher eigenvalues/eigenfunctions, $n_x, n_y, n_z \gg 1$. The recovered eigenvalues are compared with the analytical solution of this problem in the domain $\Omega = \{x \in [-1, 1]\} \times \{y \in [-1, 1]\} \times \{z \in [-1, 1]\}$ [34]. Such solution is the following:

$$\lambda^2_{n_x, n_y, n_z} = \frac{\pi^2}{4}\left[n_x^2 + n_y^2 + n_z^2\right]; \quad n_x, n_y, n_z = 1, 2, 3, \ldots \tag{30}$$

Fig. 11(a) shows the convergence history of a high eigenvalue $(\lambda^2/(\pi^2/4) = 43)$. Conclusions analogous to those reached in the two-dimensional Helmholtz eigenvalue problem and in the previously addressed applications are also drawn here. Special interest is focused on intermediate values of the order of the method, e.g. $q = 12, q = 14$. Single-precision convergence is achieved using approximately two times more discretization points than with spectral collocation methods, and double-precision convergence is achieved with less than four times more nodes than with spectral collocation methods.

For completeness, Fig. 11(b) displays the eigenfunction corresponding to the eigenvalue $(\lambda^2/(\pi^2/4) = 43)$, obtained numerically using FD-q12, showing that a non-trivial structure in terms of gradients is obtained. As with its two-dimensional analogue, reliable spatial discretization of the three-dimensional Poisson operator sets the scene for the solution of the TriGlobal eigenvalue problem.

4.5. The TriGlobal eigenvalue problem

Finally, the TriGlobal linear instability eigenvalue problem in Eq. (4) formed by the matrices (13) is solved, treating all three inhomogeneous spatial dimensions in a coupled manner.

Using the two-dimensional rectangular duct and regularized lid-driven cavity base states previously calculated, a three-dimensional, spanwise homogeneous base flow is constructed and
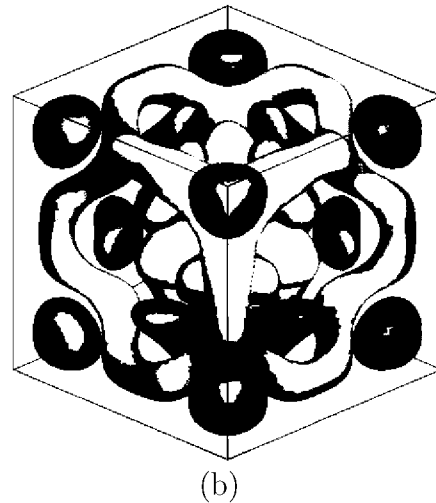

Fig. 11. (a) Convergence history of the solution of the 3D Helmholtz eigenvalue problem for the eigenvalue $\lambda^2/(\pi^2/4) = 43$, obtained using CGL and a suite of FD-q methods of orders 4, 8, 12, 16 and 20. The number of discretization nodes used is the same in the three spatial directions and is denoted by $N + 1$. (b) Iso-surfaces of the corresponding eigenfunction obtained using FD-q12 with $N_x \times N_y \times N_z = 60^3$.

analyzed by solving the three-dimensional eigenvalue problem without exploitation of the spanwise periodicity. This is the most stringent test to which the proposed spatial discretization is exposed. In view of the results, only the FD-q method is used for the solution of Eq. (4) formed by the matrices (13).

4.5.1. The rectangular duct flow

The rectangular duct flow is analyzed also with TriGlobal analysis at $Re = 1000$, employing FD-q10 in both x and y directions. For the TriGlobal analysis, N_F Fourier collocation points are used along the spanwise direction, in order to discretize a spanwise length $L_z = 2\pi/\beta_{BG}$. The parameter $\beta_{BG} = \pi$ is chosen to enable direct comparisons of the present TriGlobal with the results obtained by the solution of the BiGlobal analysis in which only (x, y) are discretized in a coupled manner. Results are presented in Table 4, where a very good agreement between BiGlobal and TriGlobal analysis results is observed: the damping rate obtained by BiGlobal analysis using the highest attainable resolution on the used desktop computer, $N_x \times N_y = 70^2$ CGL points and that delivered by the TriGlobal analysis with $N_x \times N_y = 56^2$ FD-q10 points and $N_F = 12$ Fourier collocation points, have a relative difference of $\mathcal{O}(10^{-7})$.

4.5.2. The regularized lid-driven cavity

The last test to which FD-q methods are subject is the two-dimensional regularized lid-driven cavity flow analyzed with TriGlobal analysis. For the solution of Eq. (4) formed by the matrices (13), N_F Fourier collocation points are used along the spanwise direction, in order to discretize a spanwise length $L_z = 2\pi/\beta_{BG}$, and FD-q10 in both of the x and y directions. The parameters $Re = 1000$ and $\beta_{BG} = 15$ are chosen in order to directly compare the present TriGlobal results with the results obtained with the BiGlobal analysis of Section 4.3.2. The results are presented in Table 5, where an acceptable agreement between BiGlobal and TriGlobal analysis results is observed: the damping rate obtained

Table 4
TriGlobal instability analysis of the rectangular duct flow in the domain $\Omega = \{x \in [-1, 1]\} \times \{y \in [-1, 1]\} \times \{z \in [-1, 1]\}$ at $Re = 1000$ using FD-q10 for x and y direction with $N + 1$ points and Fourier collocation with N_F points in z. The converged BiGlobal result for the same set of parameters (i.e. using $\beta = \pi$) is shown in Table 2: $\omega = 2.902765454 - i0.1035249264$. T_{LU} and T_{AR} respectively refer to time spent in the LU decomposition of the matrix and the Arnoldi iteration. Note that [†] refers to *in-core* while the rest of results are *out-of-core* calculations.

$N^2 \times N_F$	ω_r	ω_i	Memory (MB)	T_{LU} (s)	T_{AR} (s)
$32^2 \times 12$	2.90275822	−0.103516753	4862[†]	353[†]	0.8[†]
$40^2 \times 12$	2.90276481	−0.103523881	2980	1006	8.8
$48^2 \times 12$	2.90276539	−0.103524652	4611	1735	16.4
$42^2 \times 16$	2.90276510	−0.103524201	6253	3345	19.0
$56^2 \times 12$	2.90276545	−0.103524809	6539	5247	20.6

Table 5
TriGlobal instability analysis of the regularized lid-driven cavity flow in the domain $\Omega = \{x \in [0, 1]\} \times \{y \in [0, 1]\} \times \{z \in [0, 2\pi/15]\}$ at $Re = 1000$ using FD-q10 for x and y direction with $N + 1$ points and Fourier collocation with N_F points in z. The converged BiGlobal result for the same set of parameters (i.e. using $\beta = 15$) is shown in Fig. 10: $\omega = i0.108337$.

$N^2 \times N_F$	ω_i	Memory (MB)	$T_{LU}(s)$	$T_{AR}(s)$
$32^2 \times 12$	0.102726	4920[†]	377[†]	0.9[†]
$40^2 \times 12$	0.106135	3226	1447	8.8
$48^2 \times 12$	0.106903	4578	1819	15.8
$42^2 \times 16$	0.106538	6061	3097	16.5
$56^2 \times 12$	0.106804	6704	3947	25.4

by BiGlobal analysis using $N_x \times N_y = 70^2$ CGL points and the one delivered by TriGlobal analysis with $N_x \times N_y = 56^2$ FD-q10 points and $N_F = 12$ Fourier collocation points show a relative difference of $\mathcal{O}(10^{-3})$. This discrepancy is expected to improve by increasing resolutions. The degree to which this is possible for the present state-of-the-art computations is discussed next.

5. The efficiency advantages of the FD-q method

Once the accuracy of FD-q methods has been established, attention may be turned to the efficiency advantage that they offer over spectral collocation methods. The solution algorithm is based on subspace iteration in which the spatial discretization matrix is formed, stored and LU-decomposed using sparse linear algebra routines and, therefore, the sparsity pattern is the key parameter for the success of the overall algorithm. Only the FD-q spatial discretization has been monitored in terms of the memory and CPU time requirements for the serial solution of the incompressible BiGlobal EVP, on account of the superior accuracy properties of this over other finite-difference methods of the same formal order (and sparsity pattern). A visual indication of the savings expected by using a given FD-q method over the CGL spatial discretization is offered by the sparsity patterns resulting from spatial discretization of the left-hand-side BiGlobal matrix $\mathcal{A}_{2D}$ of Eq. (10), respectively shown in Fig. 12(a) for CGL and Fig. 12(b) for FD-q4, both plotted using $N = 20$. The key parameter when a sparse solver is used is the Number of Non-Zero elements (NNZ). For the differential operators of this work, this parameter is reduced by a factor of $\mathcal{O}((q + 1)/(N + 1))$, with q the order of the used finite-difference scheme (i.e. $q + 1$ is the stencil of the scheme) and $N + 1$, the number of points used to discretize the problem in each spatial direction for all the differentiation matrices.[1]

The computational requirements of the overall numerical solution of the EVP are imposed by those of the LU-decomposition of the sparse matrix. The required memory and elapsed time for this factorization cannot be predicted *a priori* and the ratio $((q + 1)/(N + 1))$, elevated to a power to be determined later, is used next to relate the required memory and elapsed time of the LU-decomposition of FD-q with those of CGL spatial discretization. The flow instability problem chosen to study computational requirements is one in which all velocity components and their derivatives need to be discretized: the attachment line boundary layer (see Section 4.3.3). Spatial discretization methods used are the CGL discretization working in dense (results taken from [70]) and comparing them with the respective results corresponding to sparse CGL, FD-q8, FD-q16 and FD-q24 spatial discretizations. For this problem, $N = N_x = N_y$, so the leading dimension of the matrix operator is $M = 4(N + 1)^2$.

Table 6 shows the required memory for the LU decomposition of the BiGlobal EVP matrix using dense and sparse routines in conjunction with CGL discretization, as well as three members of the FD-q family and sparse linear algebra. The quantity of required memory when working in sparse is significantly reduced respect to the quantity of required memory working in dense, which is theoretically Mem $\approx \mathcal{O}(M^2) \approx \mathcal{O}(N^4)$. The memory requirements of the FD-q8 method are found to be smaller by one order of magnitude compared with those of the CGL method. In order to obtain a relation between the respective quantities the formula

$$\text{Mem}_{\text{FD-q}} = \left(\frac{q + 1}{N + 1}\right)^a \times \text{Mem}_{\text{CGL}} \tag{31}$$

---

[1] For the more stringent case of compressible BiGlobal instability analyses, or when non-orthogonal curvilinear mappings are used to discretize the problem, cross-derivatives are present in the differential operators. In this case, NNZ is reduced by a factor of $\mathcal{O}(((q + 1)/(N + 1))^2)$.
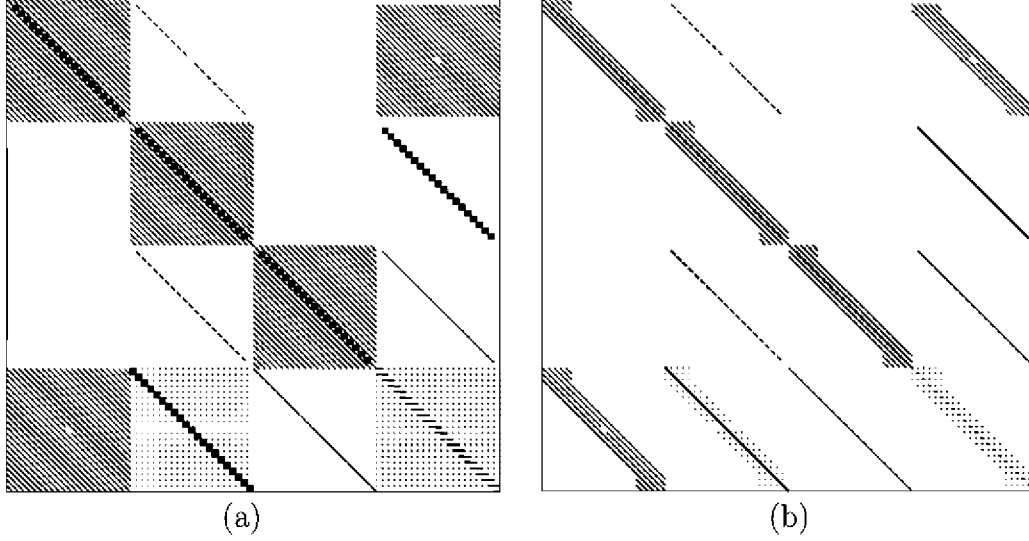
Fig. 12. Sparsity pattern of the left-hand-side BiGlobal operator matrix with $N + 1 = 21$ discretization points per spatial direction using (a) CGL and (b) FD-q4 in the attachment line boundary layer problem. (blue) Real part and (red) imaginary part of the non-zero elements. (For interpretation of the references to colour in this figure legend, the reader is referred to the web version of this article.)

Table 6
Memory requirements for the LU decomposition (MB) in the attachment line boundary layer problem, using different resolutions and working with dense algebra for CGL and sparse algebra for CGL, FD-q24, FD-q16 and FD-q8. Note that $N = N_x = N_y$.

N	CGL$_{dense}$	CGL$_{sparse}$	FD-q24	FD-q16	FD-q8
40	760	584	444	246	107
50	1747	1350	705	457	179
60	3494	3078	1217	775	284
70	6230	5544	1889	1174	436

is assumed and used to identify (fit) the constant exponent a using the results of Table 6, plotted in Fig. 13(a). Independently both the CGL and the FD-q results are taken to follow a curve Mem $\propto (N + 1)^{\alpha}$. This exponent is $\alpha_{CGL} = 4.1$ for the sparse CGL method, which is very close to the theoretical exponent of 4 for dense computations, while the values $2.7, 2.8$ and 2.6 have been identified for FD-q24, FD-q16 and FD-q8, respectively. Using the average between the three FD-q cases, $\alpha_{FD-q} = 2.7$, the constant exponent of Eq. (31) is approximated by $a = \alpha_{CGL} - \alpha_{FD-q} = 1.4$.

Fig. 13(b) shows the collapse of all FD-q curves using Eq. (31) and these constant values. The required memory for FD-q scales as Mem$_{FD-q} \approx \mathcal{O}(N^{2.7}) \approx \mathcal{O}(M^{1.3})$, which outperforms computations using CGL, the latter scaling as Mem$_{CGL} \approx \mathcal{O}(M^2)$.

Turning to the elapsed time for serial LU factorization of the matrix pertinent to the same global stability EVP, results in Table 7 are presented for the same methods. The theoretical prediction of $\mathcal{O}(M^3) \approx \mathcal{O}(N^6)$ is verified by the CGL either sparse or dense results. The most striking result of this table is the order (s) of magnitude decrease of CPU time that the FD-q method offers, when compared with either of the CGL sparse or dense solution.

In order to quantify the relation between the elapsed times required by the CGL and the FD-q methods, the formula

$$\text{Time}_{FD-q} = \left(\frac{q+1}{N+1}\right)^b \times \text{Time}_{CGL} \tag{32}$$

is assumed and used to fit the constant exponent b. Fig. 14(a) shows the results of Table 7. As in the case of memory requirements, either method is taken to follow a curve Time $\propto (N + 1)^{\beta}$. For the CGL
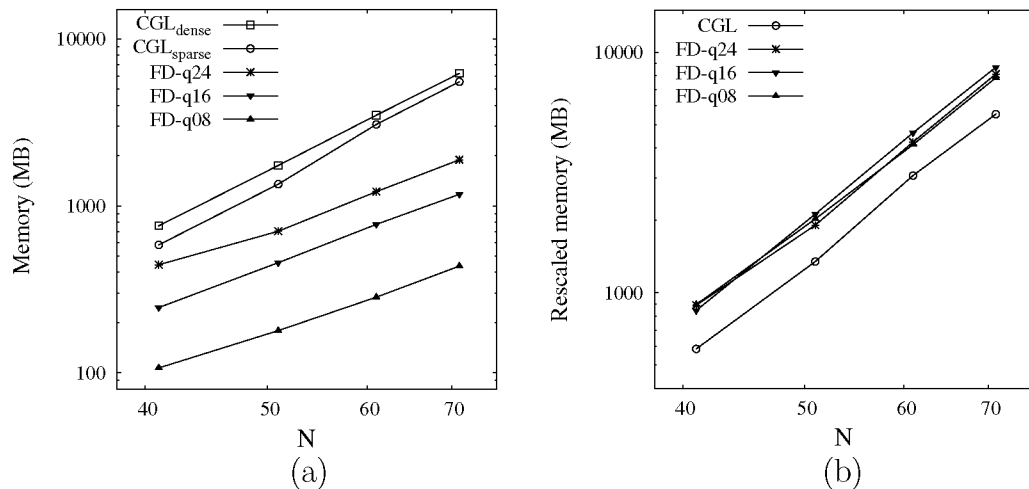

Fig. 13. (a) Required memory for LU-factorization and (b) rescaled memory using the Eq. (31) versus number of discretization points per direction, $N + 1$.

N	CGL$_{dense}$	CGL$_{sparse}$	FD-q24	FD-q16	FD-q8
40	152.7	34.7	18.0	7.6	2.0
50	553.9	97.0	33.1	16.8	3.6
60	1603.4	292.0	80.2	35.2	6.3
70	4665.8	516.3	136.8	57.3	10.8

method the exponent extracted from the results is $\beta_{CGL} = 6.0$, which is exactly the theoretical exponent for dense calculations, while the exponent values of 3.8, 3.7 and 3.1 have been obtained for FD-q24, FD-q16 and FD-q8, respectively. Again, using the average value of the three FD-q cases, $\beta_{FD-q} = 3.5$, the constant exponent of Eq. (32) is approximated by $b = \beta_{CGL} - \beta_{FD-q} = 2.5$. Fig. 14(b) shows the collapse of the FD-q CPU-time curves onto a single FD-q curve, which has the same slope as that obtained using CGL discretization, when Eq. (32) is used with this parameter value. Therefore, the CPU time for FD-q scales as Time$_{FD-q} \approx \mathcal{O}(N^{3.5}) \approx \mathcal{O}(M^{1.7})$, instead of Time$_{CGL} \approx \mathcal{O}(M^3)$ for CGL.

The reductions in computational effort by the sparse solution of the BiGlobal eigenvalue problem in which the matrix is formed using the FD-q methods are made palpable by recalling the largest such solution to-date, namely the massively parallel computations of Kitsios et al. [24] and Rodríguez and Theofilis [26]. The latter work was performed on the JUGENE supercomputing facility [71], on which 2048 processors were used in order to distribute the 1 TB large matrix resulting from the CGL spectral collocation discretization of the incompressible operator on a $N_x \times N_y = 250^2$ grid, employing the parallel dense linear algebra library ScaLAPACK [72], with an elapsed time of ≈ 10.5 hours of wall-clock time (≈ 22000 total hours of CPU time). Using the BiGlobal results of Fig. 10 as a guidance, and employing the relation $N_{CGL} \approx 2N_{FD-q8}$ at which the CGL and the FD-q8 spatial discretizations both reach a relative error of $\varepsilon_\omega \approx 10^{-5}$ in the leading eigenmode, the results of [24,26] could be obtained by employing $N_x \times N_y = 500^2$ FD-q8 points. The memory estimation provided by the sparse direct solver MUMPS on a serial desktop is 28 GB for *in-core* and 3.2 GB for *out-of-core* calculations. The estimation of the respective elapsed time is calculated by extrapolating the results of Table 7 for CGL sparse results to $N = 500$ with the previously calculated slope $\beta_{CGL} = 6.0$, resulting Time$_{CGL} \approx 18000$ CPU hours, and then using Eq. (32) to obtain the estimation of Time$_{FD-q8} \approx 46$ CPU minutes.

In order to complete the cost estimations, the relation $N_{CGL} \approx 4N_{FD-q8}$, observed in the results of Fig. 8 at which the CGL and the FD-q8 spatial discretizations both reach a relative error of $\varepsilon_\lambda \approx 10^{-9}$ in the leading eigenmode, is adopted. Now, using $N_{FD-q8} = 1000$, the memory estimation provided by MUMPS is 137 GB for *in-core* and 13.3 GB for *out-of-core* calculations. For the time estimation, following the same procedure, the result of Time$_{FD-q8} \approx 9$ CPU hours is obtained. While these estimates are one order of magnitude larger than those corresponding to $N_x \times N_y = 500^2$ FD-q8 collocation nodes, the FD-q methods still offer an interesting alternative to the commonly employed spectral collocation methods for this class of stability problems.

6. Conclusions

The prime consideration in performing numerical solutions of the linear flow instability eigenvalue problems is accuracy. Following the influential work of Orszag [49], spectral spatial discretization has historically been the method of choice for spatial discretization of the linear local stability analysis operator, a tendency which to a large extent continues presently in the context of global linear flow instability analysis. The present contribution has presented a comparison of a suite of high-order finite-difference spatial discretizations of the linear stability operator in regular Cartesian two- and three-dimensional domains and compared the respective results against those delivered by standard multi-dimensional spectral collocation discretization of the same spatial operators. The FD-q method [32] has been found to outperform all its peers at any given formal order of accuracy, and tend toward the spectral results in the limit of the bandwidth of the differentiation matrix being equal with the leading matrix dimension, $q \to N$. Exploiting the sparsity at $q \ll N$, accurate results have been delivered at orders of magnitude less storage and serial CPU time requirements, compared with the standard spectral collocation approach based on the (unmapped or mapped) Chebyshev Gauss–Lobatto grid. This permits a drastic reduction of the computing hardware on which state-of-the-art global linear instability analyses are performed when the spatial discretization matrix is stored and LU-decomposed. Results obtained demonstrate a memory reduction from $\mathcal{O}(M^2)$ to $\mathcal{O}(M^{1.3})$, being M the leading dimension of the matrix operator, as well as a reduction of CPU time from $\mathcal{O}(M^3)$ to $\mathcal{O}(M^{1.7})$. Subsequently, the usage of FD-q delivers a speedup of $\mathcal{O}(10^4)$ and a memory reduction of $\mathcal{O}(10^3)$ in the most challenging global linear stability calculation made so far using matrix formation [24,26], which used spectral collocation methods
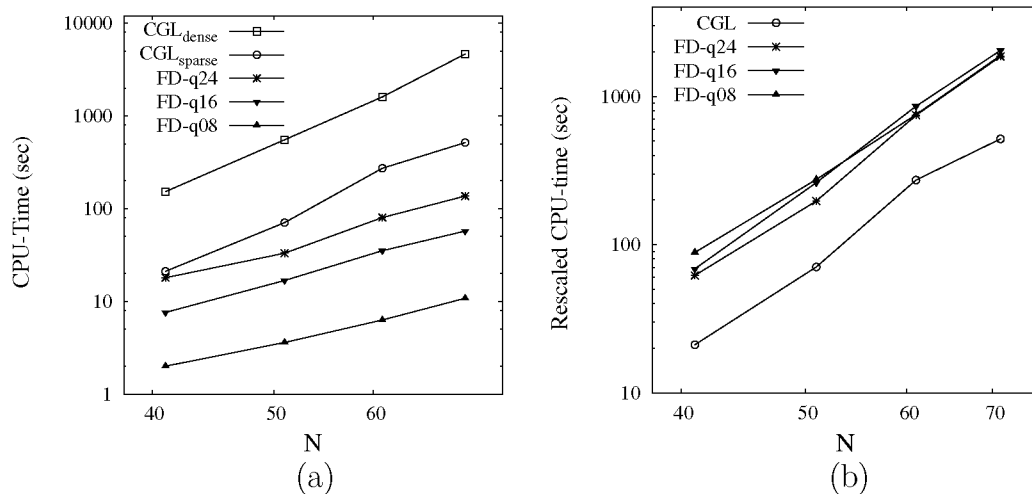

Fig. 14. (a) Elapsed time for LU-factorization and (b) rescaled CPU-time using the Eq. (32) versus number of discretization points per direction, $N + 1$.

for the spatial discretization. Both improvements permit performing TriGlobal linear instability analyses on a modern desktop with modest computational effort.

All work performed has focused on regular single-domain discretization. The question could be raised whether employing spectral multidomain or spectral element discretizations might make the CGL method against which the FD-q results have been compared more competitive. Should such a comparison be sought, one could speculate that spatial tessellations analogous to those employed by the spectral element method could be constructed and employed using FD-q spatial discretization, since the limit of the latter is spectral collocation. Such an exercise is currently in progress and results will be presented in due course.

Disclosure Statement

No conflict of interest exists for any of the authors, that could inappropriately influence, or be perceived to influence, their work. P.P. has participated in the development and validation of the different stability codes employed in this work, has obtained global instability results and collaborated in the article preparation. S.L.C. has developed finite-difference closures for the Padé and DRP schemes of various orders and obtained local instability analysis results. M.H. has provided guidance in the construction of the FD-q operators and participated in the article preparation. V.T. has participated in the selection of the test cases presented and the article preparation.

Acknowledgments

Appendix A. Dispersion-Relation-Preserving Finite Difference Schemes

Using the following notation for the first and second derivative,

$$f' = \mathcal{D}_x f, \tag{A.1}$$
$$f'' = \mathcal{D}_{xx} f, \tag{A.2}$$

the matrix formulation for the first and second derivative matrix of the DRP scheme of order 8 are given in Eq. (A.3) and (A.4) respectively.

The coefficients for the first derivative matrix $\mathcal{D}_x$ in a order 8 scheme are

$a_0 = 0,$
$a_1 = -a_{-1} = 0.85710439841850,$
$a_2 = -a_{-2} = -0.2652621696215,$
$a_3 = -a_{-3} = 0.07480520850713,$
$a_4 = -a_{-4} = -0.01444845684162,$
$a_5 = -a_{-5} = 0.00135962853377,$

and for the second derivative matrix $\mathcal{D}_{xx}$ are

$b_0 = -2.97144896555410,$
$b_1 = b_{-1} = 1.70352228610990,$
$b_2 = b_{-2} = -0.25915559206280,$
$b_3 = b_{-3} = 0.04758017242037,$
$b_4 = b_{-4} = -0.00671534695761,$
$b_5 = b_{-5} = 0.00049296326719.$

$$
\mathcal{D}_x =
\begin{pmatrix}
a_{10} & a_{11} & a_{12} & a_{13} & a_{14} & a_{15} & a_{16} & a_{17} & a_{18} & 0 & \dots & \dots & \dots & \dots & 0 \\
a_{20} & a_{21} & a_{22} & a_{23} & a_{24} & a_{25} & a_{26} & a_{27} & a_{28} & 0 & \dots & \dots & \dots & \dots & 0 \\
a_{30} & a_{31} & a_{32} & a_{33} & a_{34} & a_{35} & a_{36} & a_{37} & a_{38} & 0 & \dots & \dots & \dots & \dots & 0 \\
a_{40} & a_{41} & a_{42} & a_{43} & a_{44} & a_{45} & a_{46} & a_{47} & a_{48} & 0 & \dots & \dots & \dots & \dots & 0 \\
a_{50} & a_{51} & a_{52} & a_{53} & a_{54} & a_{55} & a_{56} & a_{57} & a_{58} & 0 & \dots & \dots & \dots & \dots & 0 \\
a_{j-5} & a_{j-4} & a_{j-3} & a_{j-2} & a_{j-1} & a_j & a_{j+1} & a_{j+2} & a_{j+3} & a_{j+4} & a_{j+5} & 0 & \dots & \dots & 0 \\
0 & a_{j-5} & a_{j-4} & a_{j-3} & a_{j-2} & a_{j-1} & a_j & a_{j+1} & a_{j+2} & a_{j+3} & a_{j+4} & a_{j+5} & 0 & \dots & 0 \\
\dots & \dots & \dots & \dots & \dots & \dots & \dots & \dots & \dots & \dots & \dots & \dots & \dots & \dots & \dots \\
0 & \dots & 0 & a_{j-5} & a_{j-4} & a_{j-3} & a_{j-2} & a_{j-1} & a_j & a_{j+1} & a_{j+2} & a_{j+3} & a_{j+4} & a_{j+5} & 0 \\
0 & \dots & \dots & 0 & a_{j-5} & a_{j-4} & a_{j-3} & a_{j-2} & a_{j-1} & a_j & a_{j+1} & a_{j+2} & a_{j+3} & a_{j+4} & a_{j+5} \\
0 & \dots & \dots & \dots & 0 & -a_{58} & -a_{57} & -a_{56} & -a_{55} & -a_{54} & -a_{53} & -a_{52} & -a_{51} & -a_{50} \\
0 & \dots & \dots & \dots & 0 & -a_{48} & -a_{47} & -a_{46} & -a_{45} & -a_{44} & -a_{43} & -a_{42} & -a_{41} & -a_{40} \\
0 & \dots & \dots & \dots & 0 & -a_{38} & -a_{37} & -a_{36} & -a_{35} & -a_{34} & -a_{33} & -a_{32} & -a_{31} & -a_{30} \\
0 & \dots & \dots & \dots & 0 & -a_{28} & -a_{27} & -a_{26} & -a_{25} & -a_{24} & -a_{23} & -a_{22} & -a_{21} & -a_{20} \\
0 & \dots & \dots & \dots & 0 & -a_{18} & -a_{17} & -a_{16} & -a_{15} & -a_{14} & -a_{13} & -a_{12} & -a_{11} & -a_{10}
\end{pmatrix}
\tag{A.3}
$$

$$
\mathcal{D}_{xx} =
\begin{pmatrix}
b_{10} & b_{11} & b_{12} & b_{13} & b_{14} & b_{15} & b_{16} & b_{17} & b_{18} & 0 & \dots & \dots & \dots & \dots & 0 \\
b_{20} & b_{21} & b_{22} & b_{23} & b_{24} & b_{25} & b_{26} & b_{27} & b_{28} & 0 & \dots & \dots & \dots & \dots & 0 \\
b_{30} & b_{31} & b_{32} & b_{33} & b_{34} & b_{35} & b_{36} & b_{37} & b_{38} & 0 & \dots & \dots & \dots & \dots & 0 \\
b_{40} & b_{41} & b_{42} & b_{43} & b_{44} & b_{45} & b_{46} & b_{47} & b_{48} & 0 & \dots & \dots & \dots & \dots & 0 \\
b_{50} & b_{51} & b_{52} & b_{53} & b_{54} & b_{55} & b_{56} & b_{57} & b_{58} & 0 & \dots & \dots & \dots & \dots & 0 \\
b_{j-5} & b_{j-4} & b_{j-3} & b_{j-2} & b_{j-1} & b_j & b_{j+1} & b_{j+2} & b_{j+3} & b_{j+4} & b_{j+5} & 0 & \dots & \dots & 0 \\
0 & b_{j-5} & b_{j-4} & b_{j-3} & b_{j-2} & b_{j-1} & b_j & b_{j+1} & b_{j+2} & b_{j+3} & b_{j+4} & b_{j+5} & 0 & \dots & 0 \\
\dots & \dots & \dots & \dots & \dots & \dots & \dots & \dots & \dots & \dots & \dots & \dots & \dots & \dots & \dots \\
\dots & \dots & \dots & \dots & \dots & \dots & \dots & \dots & \dots & \dots & \dots & \dots & \dots & \dots & \dots \\
0 & \dots & 0 & b_{j-5} & b_{j-4} & b_{j-3} & b_{j-2} & b_{j-1} & b_j & b_{j+1} & b_{j+2} & b_{j+3} & b_{j+4} & b_{j+5} & 0 \\
0 & \dots & \dots & 0 & b_{j-5} & b_{j-4} & b_{j-3} & b_{j-2} & b_{j-1} & b_j & b_{j+1} & b_{j+2} & b_{j+3} & b_{j+4} & b_{j+5} \\
0 & \dots & \dots & \dots & 0 & b_{58} & b_{57} & b_{56} & b_{55} & b_{54} & b_{53} & b_{52} & b_{51} & b_{50} \\
0 & \dots & \dots & \dots & 0 & b_{48} & b_{47} & b_{46} & b_{45} & b_{44} & b_{43} & b_{42} & b_{41} & b_{40} \\
0 & \dots & \dots & \dots & 0 & b_{38} & b_{37} & b_{36} & b_{35} & b_{34} & b_{33} & b_{32} & b_{31} & b_{30} \\
0 & \dots & \dots & \dots & 0 & b_{28} & b_{27} & b_{26} & b_{25} & b_{24} & b_{23} & b_{22} & b_{21} & b_{20} \\
0 & \dots & \dots & \dots & 0 & b_{18} & b_{17} & b_{16} & b_{15} & b_{14} & b_{13} & b_{12} & b_{11} & b_{10}
\end{pmatrix}
\tag{A.4}
$$

Appendix B. Compact finite difference schemes

Using the following notation for the first and second derivative

$$\mathcal{A}f' = \mathcal{B}f \Rightarrow f' = \mathcal{A}^{-1}\mathcal{B}f, \tag{B.1}$$
$$\mathcal{A}f'' = \mathcal{M}f \Rightarrow f'' = \mathcal{A}^{-1}\mathcal{M}f, \tag{B.2}$$

and taking into account the next relation for simplicity, $d = -2(b/4 + a)$, the matrix operators of the Eqs. (B.1) and (B.2) for the Padé compact scheme of order 8 are

$$
\mathcal{A} =
\begin{pmatrix}
1 & \alpha_1 & 0 & 0 & 0 & 0 & \dots & \dots & \dots & 0 \\
\alpha_2 & 1 & \alpha_2 & 0 & 0 & 0 & \dots & \dots & \dots & 0 \\
\beta & \alpha & 1 & \alpha & \beta & 0 & \dots & \dots & \dots & 0 \\
0 & \beta & \alpha & 1 & \alpha & \beta & 0 & \dots & \dots & 0 \\
\dots & \dots & \dots & \dots & \dots & \dots & \dots & \dots & \dots & \dots \\
\dots & \dots & \dots & \dots & \dots & \dots & \dots & \dots & \dots & \dots \\
0 & \dots & \dots & 0 & \beta & \alpha & 1 & \alpha & \beta & 0 \\
0 & \dots & \dots & \dots & 0 & \beta & \alpha & 1 & \alpha & \beta \\
0 & \dots & \dots & \dots & 0 & 0 & 0 & \alpha_2 & 1 & \alpha_2 \\
0 & \dots & \dots & \dots & 0 & 0 & 0 & 0 & \alpha_1 & 1
\end{pmatrix}
$$

$$\mathcal{B} = \begin{pmatrix} a_{10} & a_{11} & a_{12} & a_{13} & a_{14} & a_{15} & a_{16} & a_{17} & 0 & \dots & 0 \\ a_{20} & a_{21} & a_{22} & a_{23} & a_{24} & a_{25} & a_{26} & 0 & 0 & \dots & 0 \\ -b/4 & -a/2 & 0 & a/2 & b/4 & 0 & 0 & 0 & 0 & \dots & 0 \\ 0 & -b/4 & -a/2 & 0 & a/2 & b/4 & 0 & 0 & 0 & \dots & 0 \\ \dots & \dots & \dots & \dots & \dots & \dots & \dots & \dots & \dots & \dots & \dots \\ \dots & \dots & \dots & \dots & \dots & \dots & \dots & \dots & \dots & \dots & \dots \\ 0 & \dots & 0 & 0 & 0 & -b/4 & -a/2 & 0 & a/2 & b/4 & 0 \\ 0 & \dots & 0 & 0 & 0 & 0 & -b/4 & -a/2 & 0 & a/2 & b/4 \\ 0 & \dots & 0 & 0 & -a_{26} & -a_{25} & -a_{24} & -a_{23} & -a_{22} & -a_{21} & -a_{20} \\ 0 & \dots & 0 & -a_{17} & -a_{16} & -a_{15} & -a_{14} & -a_{13} & -a_{12} & -a_{11} & -a_{10} \end{pmatrix}$$

$$\mathcal{M} = \begin{pmatrix} m_{10} & m_{11} & m_{12} & m_{13} & m_{14} & m_{15} & m_{16} & m_{17} & 0 & \dots & 0 \\ m_{20} & m_{21} & m_{22} & m_{23} & m_{24} & m_{25} & m_{26} & 0 & 0 & \dots & 0 \\ b/4 & a & d & a & b/4 & 0 & 0 & 0 & 0 & \dots & 0 \\ 0 & b/4 & a & d & a & b/4 & 0 & 0 & 0 & \dots & 0 \\ \dots & \dots & \dots & \dots & \dots & \dots & \dots & \dots & \dots & \dots & \dots \\ \dots & \dots & \dots & \dots & \dots & \dots & \dots & \dots & \dots & \dots & \dots \\ 0 & \dots & 0 & 0 & 0 & b/4 & a & d & a & b/4 & 0 \\ 0 & \dots & 0 & 0 & 0 & 0 & b/4 & a & d & a & b/4 \\ 0 & \dots & 0 & 0 & m_{26} & m_{25} & m_{24} & m_{23} & m_{22} & m_{21} & m_{20} \\ 0 & \dots & 0 & m_{17} & m_{16} & m_{15} & m_{14} & m_{13} & m_{12} & m_{11} & m_{10} \end{pmatrix}$$

The first derivative coefficients for a Padé compact scheme of order 8 (see [28] for more details) are

$$\alpha = 4/9, \quad \beta = 1/36,$$

and the second derivative coefficients for the same order 8:

$$\alpha = 344/1179, \quad \beta = \frac{38\alpha - 9}{214}.$$

The boundary coefficients follow a special treatment. The formulation for the first and last rows of the first derivative of order 8 is

$$f'_j + \alpha_1 f'_{j+1} = \frac{1}{\Delta x} \sum_{j=1}^{M} a_j f_j, \tag{B.3}$$

with

$$\sum_{j=0}^{M} a_j = 0, \quad \sum_{j=0}^{M} a_j j = 1 + \alpha, \quad \sum_{j=0}^{M} a_j j^\gamma = \gamma \alpha_1,$$

where $M = 7$ and $\gamma = 2, 4, 6$. The second and last but one rows have the next formulation,

$$\alpha_2 f'_{j-1} + f'_j + \alpha_2 f'_{j+1} = \frac{1}{\Delta x} \sum_{j=-1}^{M} a_j f_j, \tag{B.4}$$

with

$$\sum_{j=N}^{M} a_j = 0, \quad \sum_{j=N}^{M} j a_j = 1 + 2\alpha, \quad \sum_{j=N}^{M} \frac{j^\gamma a_j}{\gamma!} = 0, \quad \sum_{j=N}^{M} \frac{j^\sigma a_j}{\sigma!} = \frac{2\alpha_2}{(\sigma - 1)!},$$

where $\gamma = 2, 4, 6, \sigma = 3, 5, 7, N = -1$ and $M = 5$.

The formulation for the first and last rows of the second derivative of order 8 is

$$f''_j + \alpha_1 f''_{j+1} = \frac{1}{\Delta x^2} \sum_{j=1}^{M} m_j f_j, \tag{B.5}$$

with

$$\sum_{j=0}^{M} m_j = 0, \quad \sum_{j=0}^{M} m_j j = 0, \quad \sum_{j=0}^{M} m_j j^2 = 2(1 + \alpha), \quad \sum_{j=0}^{M} m_j j^\gamma = 2\gamma \alpha_1, \tag{B.6}$$

where $M = 7$ and $\gamma = 2, 4, 6$. The second and last but one rows have the next formulation,

$$\alpha_2 f''_{j-1} + f''_j + \alpha_2 f''_{j+1} = \frac{1}{\Delta x^2} \sum_{j=-1}^{M} a_j f_j, \tag{B.7}$$

with

$$\sum_{j=N}^{M} m_j = 0, \quad \sum_{j=N}^{M} j m_j = 0, \quad \sum_{j=N}^{M} \frac{j^2 m_j}{2!} = 1 + 2\alpha, \quad \sum_{j=N}^{M} \frac{j^\gamma m_j}{\gamma!} = 0,$$

$$\sum_{j=N}^{M} \frac{j^\sigma m_j}{\sigma!} = \frac{2\alpha_2}{(\sigma - 2)!},$$

where $\gamma = 3, 5, 7, \sigma = 4, 6, N = -1$ and $M = 5$.

The first derivative coefficients for the finite difference scheme of order 8 of the first and last rows are

$$a_{10} = -503/140, \quad a_{11} = -63/20, \quad a_{12} = 21/2,$$
$$a_{13} = -35/6, \quad a_{14} = 35/12, \quad a_{15} = -21/20,$$
$$a_{16} = 7/30, \quad a_{17} = -1/42, \quad \alpha_1 = 7$$

and for the second and last but one rows are

$$a_{20} = -209/384, \quad a_{21} = -49/120, \quad a_{22} = 475/384,$$
$$a_{23} = -5/12, \quad a_{24} = 65/384, \quad a_{25} = -1/24,$$
$$a_{26} = 3/640, \quad \alpha_2 = 5/32.$$

In the case of the second derivative with the same order, the coefficients of the first and last rows are

$$m_{10} = 3647/261, \quad m_{11} = -11818/435, \quad m_{12} = 5889/580,$$
$$m_{13} = 7031/1044, \quad m_{14} = -973/174, \quad m_{15} = 141/58,$$
$$m_{16} = -3119/5220, \quad m_{17} = 113/1740, \quad \alpha_1 = 363/29,$$

and the second and last but one rows are

$$m_{20} = 585/512, \quad m_{21} = -141/64, \quad m_{22} = 459/512,$$
$$m_{23} = 9/32, \quad m_{24} = -81/512, \quad m_{25} = 3/64,$$
$$m_{26} = -3/512, \quad \alpha_2 = 11/128.$$

References

[1] V. Theofilis, Global linear instability, Annu. Rev. Fluid Mech. 43 (2011) 319–352.
[2] N. Abdessemed, S.J. Sherwin, V. Theofilis, Linear instability analysis of low pressure turbine flows, J. Fluid Mech. 628 (2009) 57–83.
[3] D. Barkley, H.M. Blackburn, S.J. Sherwin, Direct optimal growth analysis for timesteppers, Int. J. Numer. Meth. Fluids 57 (2008) 1435–1458.
[4] R.T. Pierrehumbert, Universal shortwave instability of two-dimensional eddies in an inviscid fluid, Phys. Rev. Let. 57 (1986) 2157–2159.
[5] A. Zebib, Stability of viscous flow past a circular cylinder, J. Eng. Math. 21 (1987) 155–165.
[6] T. Tatsumi, T. Yoshimura, Stability of the laminar flow in a rectangular duct., J. Fluid Mech. 212 (1990) 437–449.
[7] C.P. Jackson, A finite-element study of the onset of vortex shedding in flow past variously shaped bodies, J. Fluid Mech. (1987) 23–45.
[8] M. Morzyńksi, F. Thiele, Numerical stability analysis of flow about a cylinder, Z. Angew. Math. Mech. 71 (1991) T424–T428.
[9] H.A. Dijkstra, On the structure of cellular solutions in Rayleigh–Benard–Marangoni flows in small-aspect-ratio containers, J. Fluid Mech. 243 (1992) 73–102.
[10] L.M. González, V. Theofilis, R. Gomez-Blanco, Finite element methods for viscous incompressible BiGlobal instability analysis on unstructured meshes, AIAA J. 45 (2007) 840–854.
[11] D. Barkley, R.D. Henderson, Three-dimensional Floquet stability analysis of the wake of a circular cylinder, J. Fluid Mech. 322 (1996) 215–241.
[12] R.D. Henderson, D. Barkley, Secondary instability of the wake of a circular cylinder, Phys. Fluids 8 (1996) 65–112.

[13] G.E. Karniadakis, S.J. Sherwin, Spectral/hp Element Methods for Computational Fluid Dynamics, second ed., Oxford University Press, 2005.

[14] V. Theofilis, D. Barkley, S.J. Sherwin, Spectral/hp element technology for flow instability and control, Aero. J. 106 (2002) 619–625.

[15] R.T. Pierrehumbert, S.E. Widnall, The two- and three-dimensional instabilities of a spatially periodic shear layer, J. Fluid Mech. 114 (1982) 59–82.

[16] L.E. Eriksson, A. Rizzi, Computer-aided analysis of the convergence to steady state of discrete approximations to the Eler equations, J. Comp. Phys. 57 (1985) 90–128.

[17] W.S. Edwards, L.S. Tuckerman, R.A. Friesner, D.C. Sorensen, Krylov methods for the incompressible Navier-Stokes equations, J. Comp. Phys. 110 (1994) 82–102.

[18] A. Tezuka, K. Suzuki, Three-dimensional global linear stability analysis of flow around a spheroid, AIAA J. 44 (2006) 1697–1708.

[19] S. Bagheri, P. Schlatter, P.J. Schmid, D.S. Henningson, Global stability of a jet in crossflow, J. Fluid Mech. 624 (2009) 33–44.

[20] H.M. Blackburn, D. Barkley, S.J. Sherwin, Convective instability and transient growth in flow over a backward-facing step, J. Fluid Mech. 603 (2008) 271–304.

[21] V. Theofilis, Advances in global linear instability of nonparallel and three-dimensional flows, Prog. Aero. Sciences 39 (4) (2003) 249–315.

[22] J.D. Crouch, A. Garbaruk, D. Magidov, Predicting the onset of flow unsteadiness based on global instability, J. Comp. Phys. 224 (2007) 924–940.

[23] D. Rodríguez, V. Theofilis, Massively parallel numerical solution of the BiGlobal linear instability eigenvalue problem using dense linear algebra, AIAA J. 47 (2009) 2449–2459.

[24] V. Kitsios, D. Rodríguez, V. Theofilis, A. Ooi, J. Soria, BiGlobal stability analysis in curvilinear coordinates of massively separated lifting bodies, J. Comp. Phys. 228 (2009) 7181–7196.

[25] D. Rodríguez, V. Theofilis, On the birth of stall cells on airfoils, Theor. Comp. Fluid Dyn. 25 (2011) 105–118.

[26] D. Rodríguez, V. Theofilis, Structural changes of laminar separation bubbles induced by global linear instability, J. Fluid Mech. 655 (2010) 280–305.

[27] X. Merle, F. Alizard, J.-C. Robinet, Finite difference methods for viscous incompressible global stability analysis, Comput. Fluids 39 (2010) 911–925.

[28] S. Lele, Compact finite difference schemes with spectral- like resolution, J. Comp. Phys. 103 (1992) 16–42.

[29] C.K.W. Tam, J.C. Webb, Dispersion-relation-preserving finite-difference schemes for computational acoustics, J. Comp. Phys. 107 (1993) 262–281.

[30] B. Strand, Summation by parts for finite difference approximations for d/dx, J. Comp. Phys. 110 (1994) 47–67.

[31] K. Mattson, J. Nordström, Summation by parts operators for finite difference approximations of second derivatives, J. Comp. Phys. 199 (2004) 503–540.

[32] M. Hermanns, J.A. Hernández, Stable high-order finite-difference methods based on non-uniform grid point distributions, Int. J. Numer. Meth. Fluids 56 (2008) 233–255.

[33] P. Schmid, D.S. Henningson, Stability and Transition in Shear Flows, Springer, New York, 2001.

[34] P.M. Morse, H. Feshbach, Methods of Theoretical Physics, Parts I, II, McGraw-Hill, 1953.

[35] V. Theofilis, P. Duck, J. Owen, Viscous linear stability analysis of rectangular duct and cavity flows, J. Fluid Mech. 505 (2004) 249–286.

[36] X. Merle, F. Alizard, J.-Ch. Robinet, Finite difference methods for viscous incompressible global instability analysis, Comput. Fluids 39 (2010) 911–925.

[37] T. Colonius, Direct computation of aerodynamic sound generation, Ph.D. Thesis, Stanford University, 1994.

[38] M. Carpenter, J. Nordström, D. Gottlieb, Revisiting and extending interface penalties for multi-domain summation-by-parts operators, J. Sci. Comput 45 (2011) 118–150.

[39] B. Fornberg, Calculation of weights in finite difference formulas, SIAM Review 40 (1998) 685–691.

[40] F. Hildebrand, Introduction to Numerical Analysis, Dover, 1987.

[41] E. Isaacson, H. Keller, Analysis of Numerical Methods, Dover, 1994.

[42] J. Boyd, Chebyshev and Fourier spectral methods, Springer, 1989.

[43] C. Canuto, M.Y. Hussaini, A. Quarteroni, T.A. Zang, Spectral Methods in Fluid Dynamics, Springer, 1987.

[44] B. Fornberg, A Practical Guide to Pseudospectral Methods, Cambridge University Press, 1998.

[45] Y. Saad, Sparskit: A Basic Tool Kit for Sparse Matrix Computations, Version 2, NAS Systems Division, 1994.

[46] Y. Saad, Variations of Arnoldi's method for computing eigenelements of large unsymmetric matrices, Linear Algebra Appl. 34 (1980) 269–295.

[47] P. Amestoy, I. Duff, J. Koster, L'Excellent, A fully asynchronous multifrontal solver using distributed dynamic scheduling, SIAM J. Matrix Anal. A 1 (2001) 15–41.

[48] P. Amestoy, A. Guermouche, J.-Y. L'Excellent, S. Pralet, Hybrid scheduling for the parallel solution of linear systems, Parallel Comput. 2 (2006) 136–156.

[49] S. Orszag, Accurate solution of the Orr-Sommerfeld stability equation, J. Fluid Mech. 50 (1971) 689–703.

[50] N.P. Kirchner, Computational aspects of the spectral Galerkin fem for the Orr-Sommerfeld equation, Int. J. Numer. Meth. Fluids 32 (2000) 119–137.

[51] L. Mack, A numerical study of the temporal eigenvalue spectrum of the Blasius boundary layer, J. Fluid Mech. 73 (1976) 497–520.

[52] V. Theofilis, Globally-unstable flows in open cavities, AIAA Paper 2000-1965, 2000.

[53] R.-S. Lin, M.R. Malik, On the stability of attachment-line boundary layers. Part 1. The incompressible swept Hiemenz flow, J. Fluid Mech. 311 (1996) 239–255.

[54] M. Morzyński, F. Thiele, Finite element method for global stability analysis of 3D flows, AIAA Paper 2008-3865, 2008.

[55] F. Giannetti, P. Luchini, L. Marino, Linear stability analysis of three-dimensional lid-driven cavity flow. Atti del XIX Congresso AIMETA di Meccanica Teorica e Applicata, (Aras Edizioni, Ancona, Italy), Ancona 14–17 Sep. 2009, 2009, pp. 738.1–738.10.

[56] Y. Feldman, A. Gelfgat, Oscillatory instability in a 3d lid-driven flow in a cube, Phys. Fluids 22 (2010) 093602.

[57] S.C. Reddy, P.J. Schmid, D.S. Henningson, Pseudospectra of the Orr-Sommerfeld equation, SIAM J. Appl. Math. 53 (1993) 15–47.

[58] N. Kirchner, Computational aspects of the spectral Galerkin fem for the Orr-Sommerfeld equation, Int. J. Numer. Meth. Fluids 32 (2000) 119–137.

[59] G.H. Golub, C.F. van Loan, Matrix Computations, third ed., The Johns Hopkins University Press, 1996.

[60] M.R. Malik, Numerical methods for hypersonic boundary layer stability, J. Comp. Phys. 86 (1990) 376–413.

[61] L.N. Trefethen, A.E. Trefethen, S.C. Reddy, T. Driscoll, Hydrodynamic stability without eigenvalues, Science 261 (1993) 578–584.

[62] T.G. Wright, EigTool, Technical Report, 2002. Available at http://www.comlab.ox.ac.uk/pseudospectra/eigtool/.

[63] S. Albensoeder, H.C. Kuhlmann, H.J. Rath, Three-dimensional centrifugal-flow instabilities in the lid-driven-cavity problem, Phys. Fluids 13 (2001) 121–136.

[64] V. Theofilis, A. Fedorov, D. Obrist, U.C. Dallmann, The extended Görtler-Hämmerlin model for linear instability of three-dimensional incompressible swept attachment-line boundary layer flow, J. Fluid Mech. 487 (2003) 271–313.

[65] L. Rosenhead, Laminar Boundary Layers, Oxford University Press, 1963.

[66] M.J. Lighthill, in: L. Rosenhead (Ed.), Laminar Boundary Layers, Oxford University Press, pp. 72–82.

[67] U. Ghia, K.N. Ghia, C.T. Shin, High-Re solutions for incompressible flow using the Navier-Stokes equations and a multigrid method, J. Comput. Phys. 48 (1982) 387–411.

[68] R. Schreiber, H.B. Keller, Driven cavity flows by efficient numerical techniques, J. Comput. Phys. 49 (1983) 310–433.

[69] J.M. Pérez, D. Rodríguez, V. Theofilis, Linear global instability of non-orthogonal incompressible swept attachment-line boundary-layer flow, J. Fluid Mech., in press, doi: http://dx.doi.org/10.1017/jfm.2012.354.

[70] E.M. Gennaro, D. Rodríguez, M.A.F. Medeiros, V. Theofilis, Sparse techniques in global flow instability with application to compressible leading-edge flow, AIAA J., submitted for publication.

[71] http://www.fz-juelich.de/ias/jsc/en/home/home_node.html.

[72] L.S. Blackford, J. Choi, A. Cleary, A. Petitet, R.C. Whaley, J. Demmel, I. Dhillon, K. Stanley, J. Dongarra, S. Hammarling, G. Henry, D. Walker, ScaLAPACK: a portable linear algebra library for distributed memory computers – design issues and performance, http://www.netlib.org/scalapack/, 1996.